

# A Bayesian approach to strong lensing modelling of galaxy clusters

E Jullo<sup>1,2</sup>, J-P Kneib<sup>2</sup>, M Limousin<sup>3</sup>, Á Elíasdóttir<sup>3</sup>, P Marshall<sup>4</sup> and T Verdugo<sup>5</sup>

<sup>1</sup> European Southern Observatory, Alonso de Cordova, Santiago, Chile

<sup>2</sup> OAMP, Laboratoire d'Astrophysique de Marseille - UMR 6110 - Traverse du siphon, 13012 Marseille, France

<sup>3</sup> Dark Cosmology Centre, Niels Bohr Institute, University of Copenhagen, Juliane Maries Vej 30, 2100 Copenhagen, Denmark

<sup>4</sup> Physics Department, University of California, Santa Barbara, CA93106-9530, USA

<sup>5</sup> Instituto de Astronomia, UNAM, AP 70-264, 04510 Mexico DF

E-mail: ejullo@eso.org

Submitted to: “Gravitational Lensing” Focus Issue of the New Journal of Physics (invited)

**Abstract.** In this paper, we explore how well, one can recover the mass distribution in strong lensing cluster cores where different set of multiple images with different redshifts have been identified. To be able to quantify the uncertainty in the mass reconstruction, we have used a Bayesian Monte Carlo Markov Chain (MCMC) sampler (“Bayesys”). In particular, such optimization method allows to avoid local minima in the likelihood distributions which can be frequent in large parameter spaces modelling.

To illustrate the power of the MCMC technique, we have simulated three clusters of galaxies with a set of underlying galaxy-scale subhalos and a cluster-scale halo modelled with a Pseudo-Isothermal Elliptical Mass Distribution, a pseudo-elliptical Navarro, Frenk & White and a pseudo-elliptical Sérsic potential. For each of them, we study the degeneracies between the various model parameters. Indeed, the Bayesian sampler easily provides us with an accurate and straightforward estimation of the errors. In particular, we find that the mass of the galaxies can be strongly degenerated with the cluster mass for certain image configuration. For example, we find in our simulated clusters that the galaxy cut-off radius can only be recovered with at most a 20% error. Not surprisingly, we also found that the mass distribution outside the region of the multiple images is very poorly constrained. The only way to improve this status is to put external constraints on the mass distribution at large scale, using weak lensing or X-ray measurements or both, which can be easily implemented in the proposed Bayesian approach.

Finally, we show that by using the Bayesian evidence we can successfully infer the underlying mass distribution with no manual intervention. This confirms the ability of strong lensing at constraining the mass profile in the central region of galaxy clusters. Ultimately, such method applied to strong lensing clusters where a very large number of multiple images are identified may provide unique geometrical constraints on cosmology.

The implementation of the MCMC sampler used in this paper has been done in the LENSTOOL software which is publicly available.‡

‡ <http://www.oamp.fr/cosmology/lenstool/>



## 1. Introduction

In the 1980's with the advent of CCD imaging and its application to astronomy, giant gravitational arcs in galaxy cluster core were discovered by two independent teams (Lynds and Petrosian 1986; Soucail et al. 1987). The lensing hypothesis Paczynski (1987) was soon confirmed by Soucail et al. (1988) who measured a redshift for the giant arc in Abell 370 roughly twice larger than the cluster redshift. Since then, strong gravitational lensing turned from a theoretical curiosity to a powerful tool to probe the mass distribution of galaxies and cluster of galaxies. Strong gravitational lensing is produced when a distant galaxy is serendipitously aligned with a critical mass, although rare, strong lensing events are probably a few hundreds thousand over the whole sky (Cabanac et al. 2007).

To fully exploit strong gravitational lensing events one generally needs high resolution imaging coupled to deep spectroscopy to measure the redshift of both the lens and the lensed sources. By combining, *Hubble Space Telescope* images with ground-based spectroscopy on 8-10m telescopes, strong lensing has proved to be a winning strategy particularly for constraining the mass distribution of galaxies (e.g. Muñoz et al. 1998; Koopmans et al. 2006) and galaxy cluster cores (e.g. Kneib et al. 1996; Abdelsalam et al. 1998; Smith et al. 2005; Halkola et al. 2006).

Nowadays, one particular interest of strong lensing in cluster cores is to constrain the dark matter distribution in great details contrasting with the most up to date prediction of numerical simulations. For example, are we able to measure accurately the inner slope and the concentration parameter of the dark matter (DM) density profile in order to probe physical properties of DM or its link with the baryonic component (Sand 2007, and references therein)? Indeed, numerical simulations advocate for a cuspy DM slope that could be described by an NFW (Navarro et al. 1997) or a Sérsic (Sérsic 1968; Merritt et al. 2005) profile with low concentration. Observations are not yet giving definitive answer relative to the inner slope (Gavazzi et al. 2003; Sand et al. 2004; Sand 2007) or the concentration (Kneib et al. 2003; Gavazzi et al. 2003), but progress is being made steadily. For example in Abell 1689, after a long lasting disagreement about its concentration (Clowe and Schneider 2001; King et al. 2002; Bardeau et al. 2005; Broadhurst et al. 2005; Halkola et al. 2006), Limousin et al. (2007) has come to a consensus of  $c_{vir} \sim 6 - 8$  due to careful and detailed modelling. Comerford and Natarajan (2007) discuss the issues related to the determination of the concentration parameter with different techniques and compare a large compilation of galaxy clusters concentrations with numerical simulations.

Numerical studies have shown that the concentration parameter of the NFW potential is very sensitive to complex structures on the line of sight (King and Corless 2007) or triaxiality of the dark matter halos (Corless and King 2006). Improved datasets and more complex models and techniques are needed to accurately model the mass distribution of gravitational lenses. This tendency towards always more complex models is not new and has generated two competitive methods to model the lens as soon as in the late 90'.

The non-parametric methods have been developed to constrain the mass distribution of admitted well constrained lenses (Saha and Williams 1997; Abdelsalam et al. 1998) in order to probe the large diversity of possible mass models, investigating in particular the degeneracy in the measurement of the Hubble constant. Indeed, should one continue to increase the model complexity by adding additional free parameters

when the observational constraints tighten? Since 1997, non-parametric modelling has been tested on more and more lenses with more and more complex techniques to overcome the lack of constraints very common in strong lensing (e.g. Diego et al. 2005; Kochanek 2006). Indeed, if not sufficiently constrained, the non-parametric models are too flexible and fit the noise as well as the signal. In contrast, the parametric modelling advantage is double: it assumes a physical model with optimization results directly related to physical quantities and fits the model to the data with comparatively fewer free parameters than a non-parametric model.

With the advent of the ACS (Advanced Camera for Surveys) on Hubble, the number of observed multiply imaged systems (i.e. the number of constraints) in clusters of galaxies has increased significantly and made traditional techniques of optimization too involving. Indeed, the increased complexity of lens modelling translates into larger parameter space to explore, more local minima and more degeneracies between the parameters making the fit to the data an always more critical part of the modelling.

To date, we have used the gravitational lensing package LENSTOOL to perform the lens modelling (e.g. Smith et al. 2005). Given a parametrization describing the lens, this software explores the parameter space around the best fit region and reproduces the location of the observed multiple images. The first versions of the software (Kneib et al. 1993; Smith et al. 2005) were based on a downhill  $\chi^2$  minimization which has recently reached its limits with complex models. In order to face the current and future observational data, we have thus implemented a new optimization method based on a Bayesian Monte Carlo Markov Chain (MCMC) approach. We will investigate here, the merit of this new optimization method on simulated strong lensing clusters.

In the first part of the paper, we explain how to model a cluster of galaxies, how to identify systems of multiple images. Then, we describe the implementation of the Bayesian MCMC package BAYESYS (Skilling 2004) in the LENSTOOL software. In the second part, we present the performances of the Bayesian MCMC sampler by studying the degeneracies between the parameters of the Pseudo-Isothermal Elliptical Mass Distribution (PIEMD, Kassiola and Kovner (1993)), the pseudo-elliptical Navarro, Frenk & White (NFW, Golse et al. (2002)) and the pseudo-elliptical Sérsic potentials. In the last section, we use the Bayesian evidence to select the models between the NFW, the Sérsic and the Singular Isothermal Elliptical (SIE) potentials that best reproduce six sets of multiple images produced by six PIEMD models with different sizes of core. Finally, we discuss the limitations of the strong lensing modelling with LENSTOOL and discuss what one can expect to constrain from strong lensing given a set of multiple images.

Note that the LENSTOOL§ Bayesian MCMC implementation has already been used to model Abell 1689 (Limousin et al. 2006), Abell 68 (Richard et al. 2007), MS 2053 (Verdugo et al. 2007) and Abell 2390 (Jullo 2007). All our results are scaled to the flat, low matter density  $\Lambda$ CDM cosmology with  $\Omega_M = 0.3$ ,  $\Omega_\Lambda = 0.7$ . When necessary, we scale the masses and distances according to a Hubble constant  $H_0 = 70 \text{ km s}^{-1} \text{ Mpc}^{-1}$ .

§ This software is publicly available at : <http://www.oamp.fr/cosmology/lenstool>

## 2. Methodology

### 2.1. Modelling the different mass component

N-body simulations of galaxy clusters show that the subhalos mass distribution inside halos follow a Schechter function (e.g. Shaw et al. 2006). In order to model this multi-scale range of subhalos, we assume that the total potential of a halo can be decomposed into a collection of smaller subhalos potentials:

$$\phi_{tot} = \sum_i \phi_{c_i} + \sum_j \phi_{p_j} \quad (1)$$

where we distinguish the cluster-scale smooth and large potentials  $\phi_{c_i}$  (representing the dark matter and the intra-cluster gas, although the gas component can have different spatial extent than the DM component (Clowe et al. 2006) in the case of merging clusters) and the potentials  $\phi_{p_j}$  for the perturbing galaxy-scale subhalos (representing a galaxy and its dark matter halo) (Natarajan and Kneib 1997). The galaxy-scale subhalos are traced by the observed galaxies in the cluster. We assume therefore that there are no pure DM galaxy-scale subhalos in clusters. Until now, this method has produced good results in reproducing the observed systems of multiple images and in constraining the size of the galaxy-scale subhalos in clusters (e.g. Natarajan et al. 2006). Nevertheless, with the improvement in data quality and understanding of cluster mass distribution, this simple decomposition may be revisited in the future, in particular by separating the DM and X-ray gas mass components.

The above decomposition (1) between cluster-scale halos and galaxy-scale subhalos condition the way each type of potential is introduced in the model. We will now look in details into the different component implementation.

*2.1.1. Smooth cluster-scale halos* The smooth cluster-scale halos represents generally the dark matter and the intra-cluster gas. In a first approximation, all the components are mixed together in the modelled potential. Of course each component can be modelled independently provided the systems of multiple images can constrain them or by including external constraints. The number of such halos is hard to evaluate and generally one starts with a single halo – except when X-Ray observations or the distribution of the galaxies clearly show a multi-modal distribution.

The cD galaxy might be considered as the densest part of the cluster-scale halo and thus could be included in the cluster-scale halo potential. However, the centre of mass of the halo is generally different from the exact cD galaxy position (Smith et al. 2005). Therefore, the cD galaxy is frequently modelled with the galaxy-scale components or by an additional subhalo (providing that multiple images or other constraints such as velocity dispersion measurement (Sand 2007) help disentangle the 2 components).

Single halo models together with galaxy-scale subhalos are generally sufficient to reproduce the observed systems of multiple images (e.g. Abell 963, Abell 383 (Smith et al. 2005)). In case of multi-modal distribution or a clearly bad fit of the multiple images with a single halo, additional halos can be included to the model until a good fit is reached. Practically, no more than two cluster-scale halos have been used so far to achieve a good model (e.g. Abell 2218, Abell 1689), but this may change in the near future with the likely improvement of data (with more spectroscopic constraints on the redshift of multiple images, or with even better imaging such as the one expected with JWST) or when properly taking into account external constraints.

Wambsganss et al. (2005) and King and Corless (2007) have raised the issue of multiple halos along the line of sight affecting the lensing strength and the concentration parameter recovery when a NFW profile is fitted. In their simulations, this effect increases with source redshift and with the alignment of the halos along the line of sight. While not large, this effect is systematic, which means that models should be performed with consideration of these gravitational contaminations. Taking these into account, means that in practice we need to have a good understanding of the line of sight mass distribution either using spectroscopic surveys or with good photometric redshift measurements.

Each cluster-scale halo in a model is parametrized by a position on the sky ( $x_c, y_c$ ), a projected ellipticity of the mass distribution ( $\epsilon_\Sigma$ ) (see also Appendix Appendix B for the pseudo-elliptical developments of the Sérsic potential), a position angle (PA) and dynamical parameters that depend of the choice of potential profile used to describe the halo. In this paper, we consider either the SIE, NFW, PIEMD, or Sérsic profiles described by either 1, 2, 3, or 3 dynamical parameters respectively (see Table 1 for the analytic description of each potential).

*2.1.2. Galaxy-scale components* Kneib et al. (1996) demonstrated that the inclusion of galaxy-scale subhalos is necessary to boost the local projected mass and produce the observed systems of multiple images, particularly those ones near a cluster galaxy. Indeed, galaxy-scale components are required to reproduce accurately the perturbations observed in the positions and shapes of the multiple images (Meneghetti et al. 2007). These perturbations have been probed with galaxy-galaxy lensing (Natarajan and Kneib 1997; Natarajan et al. 2002) and compared to numerical cosmological models (Natarajan et al. 2006).

Theoretically, any subhalo located along the line of sight contributes to the lensing signal. The issue is to evaluate its lensing contribution to decide how to include it in the lens model. To do so, we assume that the subhalo position corresponds to the position of its luminous counterpart (the galaxy). If the galaxy is in the cluster, its lensing effect is easily measured in the thin lens framework. For a galaxy not in the cluster, we should either disregard it (if its lensing contribution is not important: e.g. if  $R_{Einstein} \ll \delta$ , where  $\delta$  is the spatial resolution of the lensing data,  $\delta \sim 0.1''$  for HST) otherwise, if  $R_{Einstein} > \delta$ , one should either just rescale the galaxy mass if it is not located in the strong-lensing region, alternatively, the galaxy needs to be included with proper multi-plane lensing techniques.

Generally, as the number of observed multiple images systems is not large enough to constrain the parameters of all the galaxy-scale subhalos, assumptions have thus to be made in order to reduce the number of free parameters. As shown for example by Koopmans et al. (2006), a strong correlation exists between light and mass profiles for elliptical galaxies in the field. Hence, we consider in a first approximation that the position, ellipticity and position angle of the galaxy-scale subhalos are equal to position, ellipticity and position angle of the galaxy light. In fact, apart from a few cases where galaxy-scale subhalos are directly involved in lensing events, galaxies just contribute to the total enclosed map as we will show in the second part of this paper. Their exact shapes are then not important. Moreover, regarding the galaxy-halo mass profile, we need scaling relations to link the total mass distribution to the light profile. Generally we can assume that the galaxy-scale subhalos present an isothermal profile with core and cut-off radius and that the subhalo mass is proportional to the galaxy luminosity. Thus, the dynamical parameters of the subhalos can be scaled by the

**Table 1.** LENSTOOL most used potentials.

SIE		
$\epsilon_\varphi$	$=$	$\epsilon_\Sigma/3$ <span style="float: right;">(<math>\epsilon_\Sigma &lt; 0.4</math>)<sup>a</sup></span>
$\rho$	$=$	$\rho_0/\tilde{R}$
$\rho_0$	$=$	$\frac{\sigma^2}{2\pi G}$
PIEMD		
$\epsilon_\varphi$	$=$	$\frac{1 - \sqrt{1 - \epsilon_\Sigma^2}}{\epsilon_\Sigma}$
$\rho$	$=$	$\frac{\rho_0}{(1 + \frac{\tilde{R}^2}{r_c^2})(1 + \frac{\tilde{R}^2}{r_{cut}^2})}$
$\rho_0$	$=$	$\frac{\sigma_\infty^2}{2\pi G r_c^2}$ <span style="float: right;">(<math>\sigma_0 \simeq \sigma_\infty/1.46</math>)<sup>b</sup></span>
NFW		
$\epsilon_\varphi$	$=$	$\epsilon_\Sigma/2.27$ <span style="float: right;">(<math>\epsilon_\varphi &lt; 0.25</math>)<sup>c</sup></span>
$\rho$	$=$	$\frac{\delta_c \rho_c}{\frac{\tilde{R}}{r_s}(1 + \frac{\tilde{R}}{r_s})^2}$
$\delta_c$	$=$	$\frac{200}{3} \frac{c^3}{\ln(1+c) - c/(1+c)}$ <span style="float: right;"><math>r_s = \frac{r_{vir}}{c}</math></span>
Sérsic		
$\epsilon_\varphi$	$=$	$\epsilon_\Sigma/3.55$ <span style="float: right;">(<math>\epsilon_\varphi &lt; 0.25</math>)</span>
$\ln\left(\frac{\Sigma}{\Sigma_e}\right)$	$=$	$-bn \left[ \left(\frac{\tilde{R}}{\tilde{R}_e}\right)^{\frac{1}{n}} - 1 \right]$
$bn$	$\simeq$	$2n - \frac{1}{3} + \frac{4}{405n} + \frac{46}{25515n^2}$ <sup>d</sup>

<sup>a</sup> Kneib et al. (1993)

<sup>b</sup> Golse (2002)

<sup>c</sup> Golse and Kneib (2002)

<sup>d</sup> Ciotti and Bertin (1999)

galaxy luminosity, following scaling relations such as:

$$\begin{cases} \sigma_0 = \sigma_0^* \left(\frac{L}{L^*}\right)^{1/4} \\ r_{core} = r_{core}^* \left(\frac{L}{L^*}\right)^{1/2} \\ r_{cut} = r_{cut}^* \left(\frac{L}{L^*}\right)^\alpha \end{cases} \quad (2)$$

The origin of the scaling relation for the central velocity dispersion  $\sigma_0$  resides in the Faber and Jackson (1976) relation, that has been found to be reliable for describing early-type cluster galaxies (see e.g. Wuyts et al. 2004; Fritz et al. 2005). The scaling relation for the cut-off radius  $r_{cut}$  depends on the choice of the exponent  $\alpha$ . Since the mass scales as  $M \propto \sigma_0^2 r_{cut}$ , the mass to light ratio scales as  $M/L \propto L^{\alpha-1/2}$ . The case  $\alpha = 1/2$  assumes that the mass-to-light ratio is constant for all the galaxies.

The case  $\alpha = 0.8$  corresponds to the fundamental plane for elliptical galaxies i.e.  $M/L \propto L^{0.3}$  (Natarajan and Kneib 1997; Jørgensen et al. 1996; Halkola et al. 2006). The core radius for a massive galaxies is generally very small, and can be neglected ( $r_{core} \sim 0$ ).

In the following, the galaxy-scale subhalos are assumed to follow a PIEMD model with a vanishing core and a constant mass-to-light ratio (as a function of galaxy luminosity). Only 2 free parameters  $r_{cut}^*$  and  $\sigma_0^*$  are needed to adjust their contribution in the model.

Obviously, if the number of constraints becomes large enough, we can vary more parameters for those galaxies near multiple images. Indeed, sometimes such galaxies can perturb multiply imaged systems and a finer model is required to reproduce the observed configurations.

In general, the sum of cluster-scale halos and galaxy-scale subhalos make the parametric modelling flexible enough so that all types of multiple image systems can be reproduced accurately.

## 2.2. Constraints

**2.2.1. Strong lensing regime** In the strong lensing regime, the light coming from a background source passing through a high density region is multiply imaged. Depending on the data quality and the source morphology, image details can be resolved or not. If one can identify light peaks within each image, then the most efficient way of identifying new constraints, is to associate the same details observed in the different multiple images into separate systems of multiple images.

In the case of smooth images (no internal structure detected), the first order moments of the light gives its centre and the PSF corrected second order moments of the light gives its ellipticity and its PA. These values are directly related to the source centre, ellipticity and PA through the lensing equations and therefore may be considered as constraints. Note however, that the ellipticity of a curved arc is generally ill defined, so this information can only be used if the images are relatively compact.

The observed flux of multiple images can also be considered as constraints, however properly computing the amplification between the different images is usually not simple, as the amplification is strongly varying across strongly lensed images. To take flux constraints of extended images, proper pixel-lensing model should be used. In this analysis, we will not consider image fluxes.

Finally, the redshift of the background source is a strong constraint. A spectroscopic determination is the best, but a photometric redshift can also be useful if sufficiently accurate (e.g.  $\delta z/(1+z) < 0.3$ ). Indeed, in LENSTOOL the photometric redshift likelihood can be introduced as a prior and optimized, even a large Gaussian width for the redshift is better than a uniform prior.

At first, the identification of multiple images is generally guided by generic geometrical lensing configurations: cusp, fold and saddle (Blandford and Narayan 1986) in the simple context of a single cluster-scale halo. Then, the perturbations due to galaxy-scale subhalos can be considered. In general, galaxies do not create a strong lensing event by themselves but may affect a multiple image produced by the cluster-scale halo. They can deflect it further away from their original position or even create a sub strong lensing event if the image falls inside the critical region of a galaxy-scale subhalo.

Another straightforward technique to identify multiple images is to compare



the galaxy colours. As lensing is achromatic, multiple images must have similar colours unless of course when one image is strongly contaminated by a nearby galaxy. Photometric redshifts can also confirm multiple image systems.

The identification process of multiple image is iterative and strongly linked to the determination of the mass profile starting from the most obvious systems close to the cluster centre and progressively adding perturbations and new systems. A new multiple image can be predicted before it is observationally confirmed.

### 2.2.2. Other lensing constraints

*Single images* Single images with a known redshift lying near the strong lensing region (typically when  $R_{Einstein} < r < 2R_{Einstein}$ ) may also constrain the lens model. Indeed, single images may help in constraining an area of a model where no multiple image system is detected. Such constraints have up to now been neglected, therefore, we propose here an efficient way to include them in the  $\chi^2$ .

The idea to take into account the single image constraint, is to add a penalizing term in the likelihood if an observed single image is seen as multiple images during the model optimization. The likelihood is penalized according to the number of images predicted and the dispersion of their positions in the image plane.

One can implement the single image constraint in the following way:

$$\chi_{single}^2(i) = n_i \frac{[x_{obs} - \langle x^j(\boldsymbol{\theta}) \rangle]^2}{\sigma_i^2}, \quad (3)$$

where  $\chi_{single}^2(i)$  is for a singly imaged source  $i$  observed at  $x_{obs}$  that would produce  $n_i$  multiple images for a given sample of parameters  $\boldsymbol{\theta}$  and  $\langle x^j(\boldsymbol{\theta}) \rangle$  is the barycentre of the  $n_i$  predicted images. In the case where only one single image is observed then  $\langle x^j(\boldsymbol{\theta}) \rangle = x_{obs}$  and  $\chi_{single}^2(i) = 0$ .

Thanks to this definition, samples of parameters that predict multiple images for an observed singly imaged source are penalized according to the number of predicted images and their dispersion on the sky. Indeed, since the Einstein radius grows proportionally to the enclosed mass, if a sample of parameters  $\boldsymbol{\theta}$  produces a too heavy cluster, then the singly imaged source becomes multiply imaged and the dispersion of the multiple images increases with the enclosed cluster mass. This  $\chi^2$  definition imposes then an upper limit on the enclosed mass at the single image position.

Since singly imaged systems only impose a limit on the model parameters, it cannot be accounted as a true constraint in the computation of the  $\chi^2$  degrees of freedom.

*Location of critical lines* The merging/creation of pairs of images (Blandford and Narayan 1986) can sometimes be directly observed. When this occurs, the corresponding critical line must pass in-between the 2 disappearing/appearing images. We can use this information to put a constrain on the lens model by minimizing the distance between the specified position and the critical line predicted by a model as shown in Fig. 1.

Given a spatial prior for the critical line position defined by a centre  $\mathbf{O}$ , a PA and an Gaussian error on the position  $\sigma_{cl}$ , the corresponding  $\chi^2$  is given by

$$\chi_{cl}^2 = \frac{\|\mathbf{O} - \mathbf{D}\|^2}{\sigma_{cl}^2}, \quad (4)$$

where  $\mathbf{D}$  is the intersection of the predicted critical line and the defined prior.

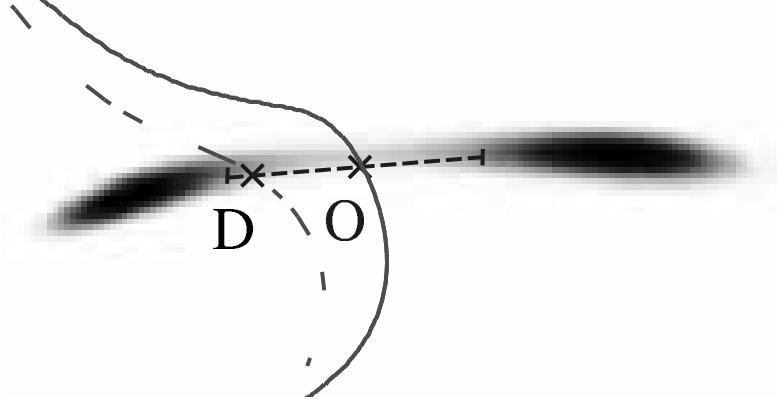


**Figure 1.** Merging of a pair of lensed images and determination of the distance between the fiducial critical line position (*solid line*) and a critical line obtained with a mock model (*dashed line*). The dashed segment represents the  $1\sigma$  prior about the critical line position.

*Weak shear signal* Outside the critical surface density region, the weak shear signal can be used to constrain the model on larger scales. Considering a catalogue of background galaxies with shape measurements, one can minimize the difference between the ellipticity of each galaxy and the reduced shear predicted by a mock model at the galaxy position. Of course, the intrinsic ellipticities of individual galaxies produce a large error when summed over the entire catalogue but this error converges to a minimum corresponding to the best model. We will discuss the weak lensing constraint implementation in a forthcoming paper.

### 2.3. Likelihood

As explained above, the standard definition of the likelihood for the multiple images (Kneib et al. 1996) can be expanded in order to include the constraints from singly imaged sources. The data considered here are the positions of the multiple and single images, we will not consider the shape parameters of images neither the weak lensing signal. Moreover, we assume that the noise associated to the measurement of the images positions is independent and Gaussian for each image, therefore the covariance matrix is diagonal. We can then use the standard definition of the likelihood function  $\mathcal{L}$  for  $N$  systems of multiple images  $D$ :

$$\mathcal{L} = \Pr(D|x(\boldsymbol{\theta})) = \prod_{i=1}^N \frac{1}{\prod_j \sigma_{ij} \sqrt{2\pi}} \exp^{-\frac{\chi_i^2}{2}}, \quad (5)$$

where the  $\chi_i^2$  for a system of  $n_i$  multiple images is

$$\chi_i^2 = \sum_{j=1}^{n_i} \frac{[x_{\text{obs}}^j - x^j(\boldsymbol{\theta})]^2}{\sigma_{ij}^2}, \quad (6)$$

where  $\boldsymbol{\theta}$  is a sample of parameters,  $x^j(\boldsymbol{\theta})$  is the predicted position of an image by this sample and  $\sigma_{ij}$  is the assumed Gaussian error on the position. The  $\chi^2$  defined here is computed in the image plane.

It is important to note that a major issue of the  $\chi^2$  computation in the image plane is to find (all) the images given a source position. Dominik (1995) proposed the minimization Powell's routine to find the roots of the lens equation. This is equivalent to any method of ray tracing that associate source plane to image plane grids. With these methods, one can find the positions of all the images but there is no simple way of associating observed and predicted images to compute the  $\chi^2$ .

In contrast, the algorithm implemented in LENSTOOL is a simplex method (Press et al. 1986) of image transport (Schneider et al. 1992). By definition, predicted and observed images are always associated. The  $\chi^2$  is thus easily computed. However, in models producing different types of multiple images systems, the method sometimes fails in predicting image positions (this is particularly true for radial images). If it is the case for a given sample of parameters, the corresponding model is simply rejected.

The MCMC method we implemented in Lenstool can be applied directly without preprocessing the parameter space to identify the best fit region. However, many models have to be tested and rejected before the Bayesian sampler (see below) focus on the best fit region. This unnecessarily increases the computation time. In this paper, we first locate the best fit region with a classical source plane optimization which is much more effective in terms of computing time (Kneib et al. 1996) and then perform the image plane optimization.

#### 2.4. Error estimation

The variance measurement  $\sigma_{ij}$  used in the likelihood above, represents the uncertainty of the location of a (multiple) image. Its accurate determination is not simple as it is a function of the S/N of the image and is not always isotropic. When the multiple images are point like,  $\sigma_{ij}$  can be estimated by the FWHM of the PSF of the observations. Within this paper, for simplicity, we assume point like images, which translates to a constant  $\sigma_{ij}$  for all images. However, in real observations, the multiple images are generally partly resolved and sometime with no point like feature, making the determination of  $\sigma_{ij}$  difficult. A possible way to then measure  $\sigma_{ij}$  is to fit for each images the surface brightness distribution of the multiple images by a 2D Gaussian distribution, thus different  $\sigma_{ij}$  for different images can be introduced in the  $\chi^2$  computation.

### 3. A Bayesian Monte Carlo Markov Chain method

We have implemented the Bayesian MCMC package BAYESYS (Skilling 2004) to perform the lens model fitting. By model, we mean the free parameters but also the fixed parameters, the mass profile, the number of halos and subhalos ... i.e. our assumptions to describe the cluster. Contrary to standard maximum likelihood methods or the previous downhill parabolic optimization method (Kneib et al. 1993), the Bayesian MCMC sampler does not look for the best sample of parameters for a model but draws the most probable samples considering the data and the knowledge we have about the unknown parameters i.e. the priors  $\Pr(\boldsymbol{\theta}|M)$  where  $\boldsymbol{\theta}$  is a sample and  $M$  is an assumed model. In LENSTOOL, we have implemented uniform and Gaussian priors. The Gaussian prior may be used when we have a previous fit with a mean value and an error around this value, or in case of external constraints (e.g. photometric redshift, orientation of the light distribution). The uniform prior is defined by a minimum and a maximum limits, with all values in-between being equi-probable.

Theoretically, the Bayesian approach is better suited than regression techniques in situations where we do not have a lot of data because the data may not provide enough constrain and an input prior is needed. Thus, it is well suited to strong lens modelling given the few constraints we generally have to optimize a model.

The Bayesian approach provides 2 levels of inference, or model comparison : the posterior and the evidence. The posterior  $\Pr(\boldsymbol{\theta}|D, M)$  is the probability distribution function (PDF) of the samples  $\boldsymbol{\theta}$  considering the data  $D$  and the model  $M$ . It will be the highest for the best fit model consistent with the priors but regardless of the model complexity. On the other hand, the evidence  $\Pr(D|M)$  is the probability of having the data  $D$  considering the model  $M$ . It measures the complexity of a model and if applied as model inference, it acts as an Occam's razor : "All things being equal, the simplest solution tends to be the best one". The reduced  $\chi^2$  analysis is only a rough approximation to the evidence analysis, although it does provide an absolute estimator of goodness-of-fit (provided the error estimates on the data are accurate).

In the Bayes theorem:

$$\Pr(\boldsymbol{\theta}|D, M) = \frac{\Pr(D|\boldsymbol{\theta}, M)\Pr(\boldsymbol{\theta}|M)}{\Pr(D|M)}, \quad (7)$$

the posterior is the joint PDF of the likelihood defined in Section 2.3 and the prior PDF divided by the evidence.

In information theory, the evidence combines the likelihood and the information  $I$ , or negative entropy

$$I = \int \Pr(\boldsymbol{\theta}|D) \log(\Pr(\boldsymbol{\theta}|D)/\Pr(\boldsymbol{\theta}))d\boldsymbol{\theta} \quad (8)$$

where  $\Pr(\boldsymbol{\theta}|D)$  is the posterior and  $\Pr(\boldsymbol{\theta})$  is the prior. We have removed the  $M$  from the equations for clarity. The entropy measures the information we have obtained through the Bayesian process after applying the likelihood to the prior. It can also be understood as the volume of the prior PDF over the posterior PDF or "a needle in a haystack" where the evidence measures the ratio of the needle's volume (the posterior PDF) to the haystack's volume (the prior PDF).

In general, the information is much bigger than unity because the "distance" between the prior and the posterior is large. For this reason, we use Markov Chains to focus progressively on to the posterior PDF inside the prior PDF.

In practice, we run 10 Markov chains at the same time and control the convergence speed with a variant of the "thermodynamic integration" technique (O Ruanaidh and Fitzgerald 1996) called *selective annealing*. At each step, a multi-chain Metropolis-Hasting algorithm (Metropolis et al. 1953; Hastings 1970) delete the Markov chains samples with the worst likelihood and duplicate the ones with the best likelihood so that we always keep 10 samples. Then, BAYESYS provides 8 engines to randomly mix the samples in the parameter space in order to maintain 10 uncorrelated Markov chains at each step. The  $n$ -dimensional parameter space is encoded with a space-filling Hilbert curve (Hilbert 1891). Thus the mixing time is evolving in  $\mathcal{O}(1)$  and not in  $\mathcal{O}(n)$  like in a standard Monte Carlo algorithm.

Even if producing new samples evolves in  $\mathcal{O}(1)$ , the final computation time still increases with the number of potentials since at each iteration, LENSTOOL computes the gradient of each of the potential included in the model optimization for each image. Therefore, the optimization process will take longer when more images and more potentials are added as constraints. In the case when the  $r_{cut}^*$  or  $\sigma_0^*$  parameters

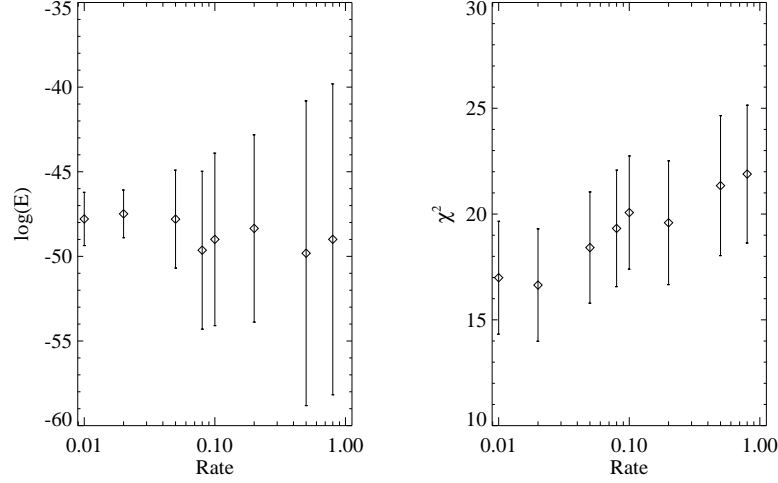


**Figure 2.** Evidence and  $\chi^2$  evolution in function of the convergence speed Rate.

are not sampled, galaxy-scale subhalos gradients are computed only once at the first iteration thus reducing the computation time drastically.

Many techniques have been proposed to compute a relevant value of the evidence. In particular, in BAYESYS, each Markov chain step is weighted by a cooling factor  $\delta_\lambda \sim \text{Rate}/(\log \mathcal{L}_{max} - \log \bar{\mathcal{L}})$  where  $\bar{\mathcal{L}}$  is the mean likelihood value of the 10 samples and Rate is a value set by the user. By decreasing Rate, the user can increase the evidence precision (see Fig. 2) whereas increasing Rate increases the convergence speed. In a first approximation, a value of 0.5 should give a rough idea of the evidence and the posterior PDF.

At the beginning of the optimization,  $\delta_\lambda$  is small because the likelihood dispersion in the 10 samples is large. The annealing process also called burn-in phase keeps the convergence as smooth and monotonically decreasing as possible, so that the evidence can be as precise as possible. Indeed, during the whole process, the evidence  $E$  is computed with:

$$\log E = \sum_{\lambda=0}^{\lambda=1} \langle \log \mathcal{L} \rangle_\lambda \delta_\lambda, \quad \text{with } \lambda = \sum \delta_\lambda. \quad (9)$$

Therefore, small values of  $\delta_\lambda$  – i.e. small values of Rate – reduce the propagation of random artifacts that can appear in the value of  $\langle \log \mathcal{L} \rangle$  making the computed evidence more reliable.

Figure 2 shows how  $\log E$  and the associated error bars evolves with the Rate value. When Rate decreases, the evidence converges towards a stable value and the errors get smaller. At Rate = 0.01,  $\sigma_{\log E} = 1.5$ . High accuracy and repeatability of the evidence is always desirable as it is an indicator of a well mixed Markov chain that has converged on the true posterior PDF. On the right panel, the mean  $\chi^2$  obtained during the sampling phase of a Bayesian run also decreases towards a stable value but the associated errors stay the same.

In the rest of this paper, we use a Rate of 0.1 unless specified. Indeed, in the parameters degeneracies study, we are not interested in comparing models so we do

not need a high precision for the evidence or the  $\chi^2$ .

*3.0.1. MCMC output* To summaries, the selective annealing process may be understood as a modified version of the Bayes theorem:

$$\Pr(\boldsymbol{\theta}|D, M) = \frac{\Pr(D|\boldsymbol{\theta}, M)^\lambda \Pr(\boldsymbol{\theta}|M)}{\Pr(D|M)}. \quad (10)$$

All along the burn-in phase, the likelihood influence is raised progressively as  $\lambda$  increases (from 0 to 1) to drive the posterior PDF from the prior PDF to its final PDF.

Once the sampler has reached  $\lambda = 1$ , there is no more samples selection through selective annealing. This means that every Markov chain is left at its place in the parameter space and moves slightly around on the Hilbert curve. Of course, the number of Markov chains sampling a given region of the posterior PDF depends of the posterior value at this place. Therefore, the most probable regions will produce more samples than the less probables ones.

The more samples we collect after the burn-in phase, the better the resolution of the posterior PDF. This is of particular interest given that we use histograms to represent the marginalized posterior PDF  $\Pr(\theta_i|M)$  with  $\theta_i$  an optimized parameter. The number of bins is intrinsically linked to the number of samples. To determine the bins sizes, we use the Freedman & Diaconis rule (Freedman and Diaconis 1981). They have shown that in order to get the best fit between a PDF and the corresponding histogram, the bin size had to be:

$$\text{Bin size} = 2\text{IQR}(\theta_i)N^{-1/3}, \quad (11)$$

where IQR is the interquartile range of the  $\theta_i$  samples and  $N$  is the number of samples.

The produced 2D posterior histograms in the rest of the paper show that the parameter distributions are not perfectly Gaussian and not independent. Techniques based on correlation matrix obtained around the best fit to measure Gaussian errors are not correct and likely underestimate some errors. Therefore care as to be taken when measuring the errors on the estimated parameters and asymmetric error bars must be adopted in case of large asymmetries observed in the posterior PDF.

To compress the posterior PDF and provide a convenient way of comparing them, we use the median and the standard deviation. It has been shown (Simard 1996) that the median is the most robust estimator for unimodal asymmetric distribution — which is usually the kind of distribution for our parameters — whereas the mean estimator is valid only assuming a Gaussian distribution. The more samples we have, the less we are affected by outliers.

#### 4. Potentials parameters degeneracies

In this section, we present the degeneracies of the 3 potentials PIEMD, NFW and Sérsic. Some of these degeneracies are already well known, others not so well, but they can easily be investigated with the Bayesian MCMC sampler. With each potential type, we simulate a cluster of galaxies that produce strong gravitational lensing. We then use the Bayesian MCMC sampler to sample the posterior distributions of the potentials parameters and highlight the degeneracies between the parameters in 2D histograms.

**Table 2.** Fiducial parameters for the 3 simulated cluster-scale components.

PIEMD	$\epsilon_\Sigma$	=	0.3	$r_{core} = 40.$ kpc
	$PA$	=	127.	$r_{cut} = 900.$ kpc
				$\sigma_0 = 950.$ km/s
NFW	$\epsilon_\phi$	=	0.2	$r_{200} = 1800.$ kpc
	$PA$	=	127.	$c = 6$
Sérsic	$\epsilon_\phi$	=	0.2	$R_e = 1500.$ kpc
	$PA$	=	127.	$\Sigma_e = 5 \cdot 10^7$ M $_\odot$ /kpc $^2$
				$n = 2.8$
$L^*$ galaxy	$r_{cut}^*$	=	18. kpc	$\sigma_0^* = 200.$ km/s

#### 4.1. Description of the simulation

**4.1.1. The mass models** The 3 simulated clusters were constructed with one cluster-scale halo and 78 galaxy-scale subhalos used to create perturbations in the lensing signal. They are distributed like the galaxies in the galaxy cluster Abell 2390 in a region of 200 kpc radius around the cluster centre which is twice larger than the radius of our outermost images.

The galaxy-scale subhalos are described by PIEMD potentials with a vanishing core radius. They are scaled with the scaling relations (2) and a constant M/L ratio. We consider the scaling parameters  $r_{cut}^* = 18$  kpc and  $\sigma_0^* = 200$  km/s values obtained through galaxy-galaxy lensing in Abell 2390 (Natarajan et al. 2006). At this redshift, the apparent K-band magnitude of an  $L^*$  galaxy is  $M^* = 17.05$  (in AB magnitude) (de Propris et al. 1999). The cluster Einstein radius for a  $z = 10$  background source is  $30''$ . The enclosed mass at this radius is  $M_{eins} = 6.7 \cdot 10^{13} M_\odot$  in which the galaxies mass contribution is about 9%. The cD galaxy is described by a truncated PIEMD potential with a vanishing core and shape parameters equal to those of its luminous counterpart. The mass profile is characterized by  $\sigma_0 = 290.$  km/s,  $r_{core} = 0$  and  $r_{cut} = 38.$  kpc.

The cluster-scale halo is described successively by the 3 potentials PIEMD, NFW and Sérsic. Their fiducial parameters are reported in Table 2.

**4.1.2. Strong lensing constraints** Three background sources  $A$ ,  $B$  and  $C$  at redshifts  $z_A = 0.6$ ,  $z_B = 1.0$  and  $z_C = 4.0$  respectively are placed in the strong lensing region of the cluster. For each mass model, we consider 3 different configurations of multiple images.

*Configuration 1:* source  $A$  is placed on the North-East side of the cluster but outside of the multiple image region. It therefore produces a single image. Also on the East side, but inside the multiple image region, source  $B$  lies along the radial caustics and produces a radial system with 3 images. On the West side, source  $C$  lies along the West naked cusp of the caustics and produces a system with 3 tangential images.

*Configuration 2:* sources  $A$  and  $C$  are at the same place but source  $B$  is placed along the East naked cusp of the caustics and produces 3 tangential images. The second configuration is therefore only constraining the enclosed mass in the outer part of the cluster ( $100 < r < 200$  kpc).

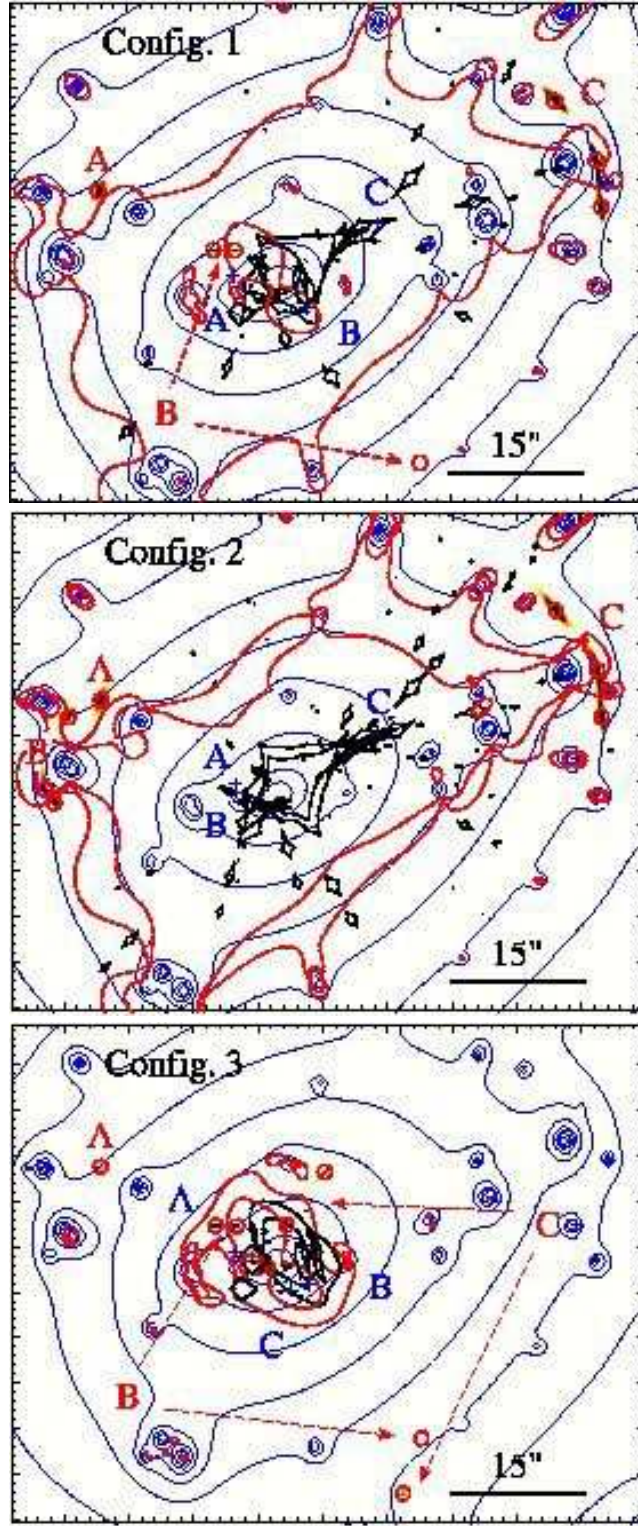


**Figure 3.** Images and sources positions of the systems  $A$ ,  $B$  and  $C$  at redshifts  $z_A = 0.6$ ,  $z_B = 1.0$  and  $z_C = 4.0$  in the configurations 1, 2 and 3. The crosses in blue mark the sources centres and the circles in red mark the images centres. The critical (caustics) curves of systems  $B$  and  $C$  are in red (black). The plotted caustics for systems  $B$  and  $C$  are radial and tangential, tangential and tangential and radial and radial respectively for Config. 1, 2 and 3. The iso-density contours of the mass profile is in blue. North is up and East is left.



*Configuration 3:* Finally, in the third configuration, sources *A* and *B* are at the same place as in the first configuration but source *C* is placed close to the radial caustics and therefore produces a second radial system of 3 images on the West side of the cluster centre. The third configuration constrains therefore preferentially the inner part of the mass profile ( $< 100$  kpc).

The source and image positions in the three configurations are presented in Figure 3 along with the two critical and caustic curves at redshift  $z_B = 1.0$  and  $z_C = 4.0$ . A Gaussian noise of FWHM  $0.1''$  is added to the images positions to mimic observational uncertainties.

In the first and the second configurations (Config. 1 and 2), the images at large radius constrain mainly the major axis of the cluster. In Config. 3, 4 images bring lots of constraints in the cluster central region on both the East and the West sides.

#### 4.2. PIEMD posteriors distribution analysis

First, we simulate the cluster-scale halo with a PIEMD potential and perform the recovery of the fiducial parameters ( $\epsilon$ , PA,  $r_{core}$ ,  $r_{cut}$  and  $\sigma_0$ ) in the three configurations of multiple images. We assume uniform priors with 50% errors around the fiducial values for these parameters. Therefore, the computed marginalized posterior distributions are merely proportional to the likelihood function. For the scaling relations of the galaxy-scale subhalos, we also allow the parameters  $\sigma_0^*$  and  $r_{cut}^*$  to vary along uniformly within 50% errors around the fiducial values. The cD galaxy parameters are kept as fixed parameters. We therefore constrain 7 free parameters with 8 constraints.

The obtained posterior distributions are plotted in Figure 4 and the estimated parameters are given in Table 3. In all the configurations, the fiducial values are well recovered but strong degeneracies appear.

First, we note that the posterior distribution in Config. 3 are more compact than in Config. 1 and 2. Every parameters except the cut-off radius are better constrained with multiple images located at the centre of the cluster.

Then, the velocity dispersion strongly correlates with the core radius and in a weaker manner with the cut-off radius to keep the Einstein radius (i.e. the enclosed mass within the Einstein radius) constant. Indeed, for a PIEMD potential, the enclosed mass is given by (Limousin et al. 2005) :

$$M_{aper}(< R) = \frac{\pi r_{cut} \sigma_0^2}{G} \left( 1 - \frac{\sqrt{r_{cut}^2 + R^2} - \sqrt{r_{core}^2 + R^2}}{r_{cut} - r_{core}} \right). \quad (12)$$

For  $R \simeq r_{core} \ll r_{cut}$  and a constant aperture mass, we easily derive  $\sigma \propto 1/\sqrt{r_{cut}}$  and notice after a few basic calculus that  $\sigma \propto \sqrt{r_{core} + \sqrt{r_{core}^2 + R^2}}$  which is equivalent to  $\sigma \propto r_{core}$  at first order when  $R \simeq r_{core} \ll r_{cut}$ .

In Config. 3, we note that the strong lensing can slightly constrain the cut-off radius even if this value is usually better constrained with the weak-lensing. This means that once the core radius and velocity dispersion are well constrained, we manage to constrain slightly the cut-off radius – the only remaining free parameter in the aperture mass expression.

The shape degeneracy between the ellipticity and the PA observed in all the configurations is related to the presence of the giant arc at large radius in Config. 1 and 2. If the ellipticity increases, the cluster mass has to rotate towards the giant

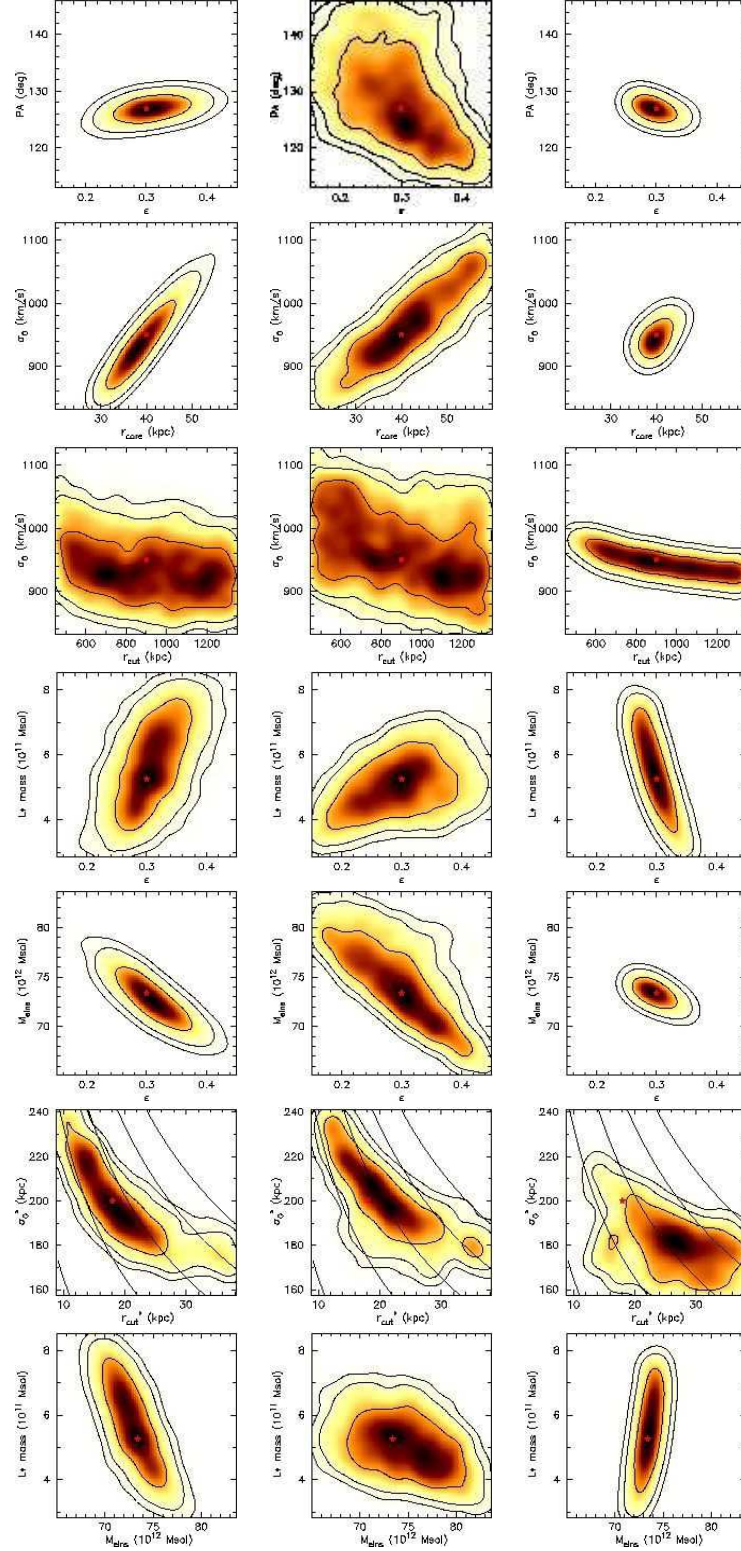


**Figure 4.** 2D Posterior distributions of the parameters of the cluster-scale halo modelled with a PIEMD potential obtained from left to right with Config. 1, 2 and 3 of multiple images respectively. The 3 contours stand for the  $1\sigma$ ,  $2\sigma$  and  $3\sigma$  levels of confidence. The fiducial values are marked by the red star. The mass of a  $L^*$  galaxy is the total mass for a circular profile. The cluster mass  $M_{\text{enc}}$  is the total enclosed mass (i.e. galaxy subhalos and cluster-scale halo) in the Einstein radius ( $30''$ ). The  $\chi^2$  was computed in the image plane.

arcs so that the enclosed mass remains the same. For Config. 2, the giant arcs are located below and above the major axis for systems *C* and *B* respectively. Therefore to maintain the enclosed mass constant at the location of the giant arcs when the ellipticity increases, the potential has to rotate clock-wise (its PA decreases) in order to get aligned with the giant arcs. However, this phenomenon is less evident with Config. 1 and 3 where the images in the cluster centre strongly constrain the potential and impede large degeneracies.

Config. 2 is particularly interesting since the variation of the ellipticity influences the PA of the cluster as well as the repartition of mass between the cluster and the galaxies. When the ellipticity decreases, the cluster mass increases and the mass of a  $L^*$  galaxy decreases i.e. the galaxies contribution to the enclosed mass at the giant arcs locations is transferred to the cluster.

This hypothesis is confirmed by the strong correlation between the cluster mass and the mass of a  $L^*$  galaxy. The more massive the cluster, the less massive the galaxies. This is expected since the multiple images constrain the total enclosed mass. However, we observe that more constraints at the cluster centre like in Config. 3 reduce this degeneracy. Indeed, the combination radial arc / counter image provides a strong constrain on the profile shape and the enclosed mass (Miralda-Escude 1995). The remaining large uncertainty in the mass of a  $L^*$  galaxy comes from the impossibility to constrain properly  $r_{cut}^*$ .

Although strong degeneracies have been highlighted between the PIEMD parameters, the aperture mass in the three configurations are similar (see Table 3).

**Table 3.** PIEMD parameters and mass estimations of the cluster-scale halo in 3 different strong lensing configurations. The parameters have been obtained with a  $\chi^2$  computed in the image plane. The errors are given at  $1\sigma$ . The  $L^*$  masses are given for a circular mass component with identical dynamical parameters.

	Fiducial	Config.1	Config.2	Config.3
$\epsilon$	0.3	0.31 $\pm 0.04$	0.30 $\pm 0.06$	0.29 $\pm 0.02$
PA (deg)	127.	127.2 $\pm 0.9$	128.5 $\pm 7.5$	127.2 $\pm 0.8$
$r_{core}$ (kpc)	40.	38.8 $\pm 4.7$	41.7 $\pm 9.3$	39.8 $\pm 1.9$
$\sigma_0$ (km/s)	950.	937.3 $\pm 43.9$	966.4 $\pm 59.8$	946.5 $\pm 16.6$
$r_{cut}$ (kpc)	900.	907.8 $\pm 253.7$	894.6 $\pm 264.7$	936.5 $\pm 235.7$
$r_{cut}^*$ (kpc)	18.	18.5 $\pm 6.5$	19.6 $\pm 6.5$	25.9 $\pm 6.3$
$\sigma_0^*$ (km/s)	200.	196.9 $\pm 16.8$	199.0 $\pm 16.5$	180.4 $\pm 12.2$
$M_{L^*}$ ( $10^{11} M_\odot$ )	5.26	5.3 $\pm 1.2$	5.1 $\pm 0.8$	5.7 $\pm 1.1$
$M_{eins}$ ( $10^{12} M_\odot$ )	73.4	73.0 $\pm 2.0$	74.6 $\pm 3.8$	73.5 $\pm 0.6$

#### 4.3. NFW posteriors distribution analysis

Now, we simulate the cluster-scale halo with a NFW potential and recover its fiducial parameters ( $\epsilon$ , PA,  $c$  and the scale radius,  $r_s$ ). We also add the 78 galaxies to the model and recover their scaling parameters  $r_{cut}^*$  and  $\sigma_0^*$  in the same manner as in the PIEMD case with the three configurations of multiple images. Again, we assume uniform priors with 50% errors for these parameters. We therefore constrain 6 free parameters with 8 constraints.

The obtained posterior distributions are plotted in Fig. 5 and the estimated parameters are reported in Table 4.

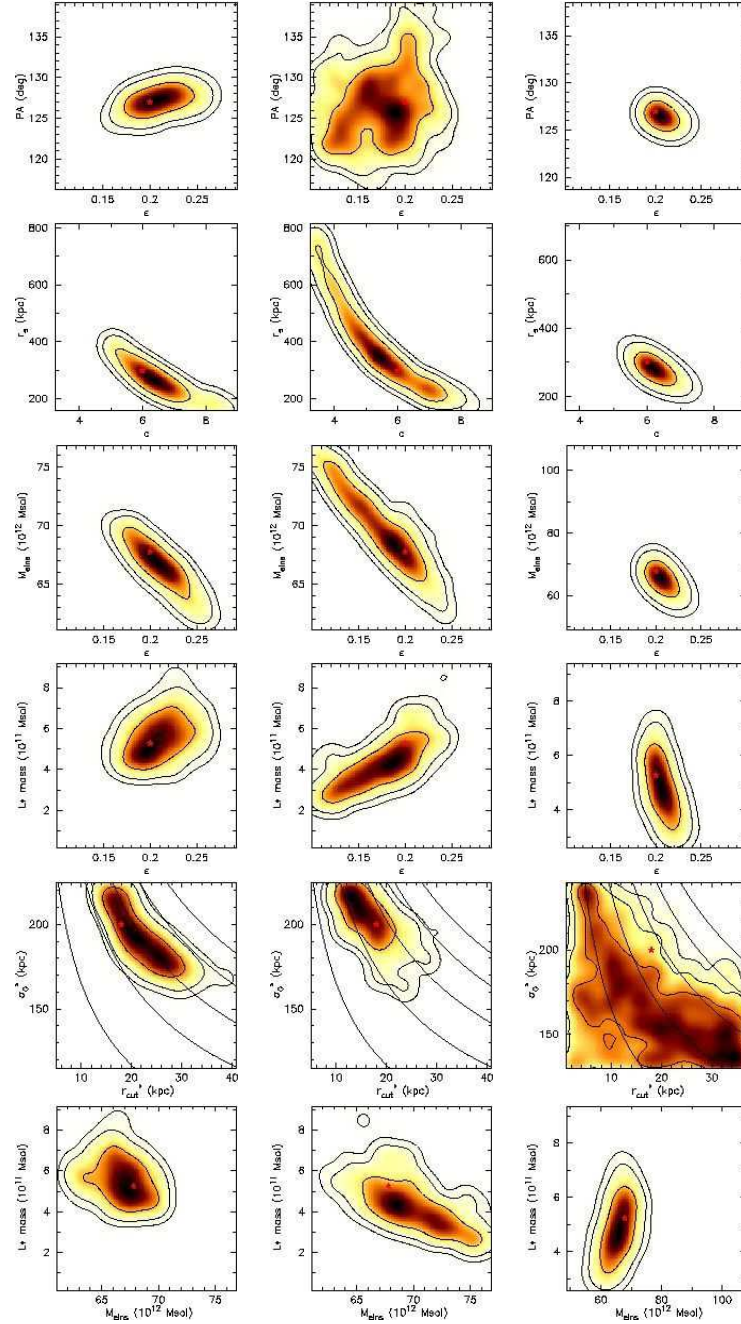


**Figure 5.** 2D Posterior distributions of the parameters of the cluster-scale halo modelled with an NFW potential obtained from left to right with Config. 1, 2 and 3 of multiple images respectively. The 3 contours stand for the  $1\sigma$ ,  $2\sigma$  and  $3\sigma$  levels of confidence. The fiducial values are marked by the red star. The mass of a  $L^*$  galaxy is the total mass for a circular profile. The cluster mass  $M_{eins}$  is the total enclosed mass (i.e. galaxy subhalos and cluster-scale halo) in the Einstein radius ( $30''$ ). The  $\chi^2$  was computed in the image plane.

Similarly to the PIEMD case, we note that the degeneracies are more compact in Config. 3 than in Config. 1 and 2 for which the central region of the cluster is less constrained.

Concerning the degeneracies in the NFW potential, we note a strong dynamical degeneracy between  $c$  and the scale radius. This degeneracy can be fitted by a power law  $r_s \propto c^\alpha$  where  $\alpha = -1.7, -1.5$  and  $-1.4$  for Config. 1, 2 and 3 respectively. This relation comes from the NFW definition of the aperture mass.

The ellipticity and the PA correlate in the same manner as in the PIEMD case. Again, it depends on the enclosed mass at the place of the giant arc and similarly as in the PIEMD case, the cluster's ellipticity correlates with the cluster mass and the mass of a  $L^*$  galaxy.

However, although the parameters are better constrained with the NFW potential than with the PIEMD potential, the mass of a  $L^*$  galaxy is still weakly constrained. In fact, the enclosed mass of the subhalos scaled with the scaling relations is

$$M_{aper}(< R) = \sigma_0^{*2} r_{cut}^* \sum_i \frac{\pi}{G} \left( \frac{L_i}{L^*} \right), \quad (13)$$

where  $L_i$  is the luminosity of a galaxy located inside the radius  $R$ . Therefore, for a constant enclosed mass,  $\sigma_0^* \propto 1/\sqrt{r_{cut}^*}$ . From the obtained results (not including the Config. 3 case), we note that  $dr_{cut}^*/r_{cut}^* \sim 5 \times d\sigma_0^*/\sigma_0^*$  on average. Of course, this strongly depends on how constrained the enclosed mass of the subhalos and the cluster-scale halo are. In particular in Config. 3, the  $L^*$  galaxy parameters are badly constrained because of the few constraints at large radius.

**Table 4.** NFW parameters and mass estimations of the cluster-scale halo in 3 different strong lensing configurations. The parameters have been obtained with a  $\chi^2$  computed in the image plane. The errors are given at  $1\sigma$ . The  $L^*$  masses are given for a circular mass component with identical dynamical parameters.

	Fiducial	Config.1	Config.2	Config.3
$\epsilon$	0.2	0.21 $\pm$ 0.02	0.18 $\pm$ 0.03	0.21 $\pm$ 0.01
$PA$ (deg)	127.	127.4 $\pm$ 1.0	126.6 $\pm$ 4.0	126.6 $\pm$ 0.6
$c$	6.	6.5 $\pm$ 0.9	6.4 $\pm$ 0.8	5.9 $\pm$ 0.3
<i>Scale radius</i> (kpc)	300.	269.3 $\pm$ 54.6	367.9 $\pm$ 149.9	284.7 $\pm$ 22.5
$r_{cut}^*$ (kpc)	18.	21.6 $\pm$ 4.8	16.3 $\pm$ 3.9	20.6 $\pm$ 3.1
$\sigma_0^*$ (km/s)	200.	191.5 $\pm$ 15.4	205.6 $\pm$ 13.4	169.6 $\pm$ 27.8
$M_{L^*}$ ( $10^{11} M_\odot$ )	5.26	5.56 $\pm$ 0.9	4.2 $\pm$ 1.1	4.9 $\pm$ 0.9
$M_{eins}$ ( $10^{12} M_\odot$ )	67.8	66.9 $\pm$ 1.8	69.5 $\pm$ 2.9	67.4 $\pm$ 0.8

#### 4.4. Sérsic posterior distribution analysis

Finally, we simulate the cluster-scale halo with a Sérsic profile and recover the parameters ( $\epsilon$ , PA,  $R_e$ ,  $\Sigma_e$  and  $n$ ) of the cluster as well as the scaling parameters  $r_{cut}^*$  and  $\sigma_0^*$  of an  $L^*$  galaxy in the same manner as in the PIEMD and NFW cases with the three configurations of multiple images. Again, we assume uniform priors with 50% errors for these parameters. We therefore constrain 7 free parameters with 8 constraints.

The obtained posterior distributions are plotted in Figure 6 and the estimated parameters are reported in Table 5.

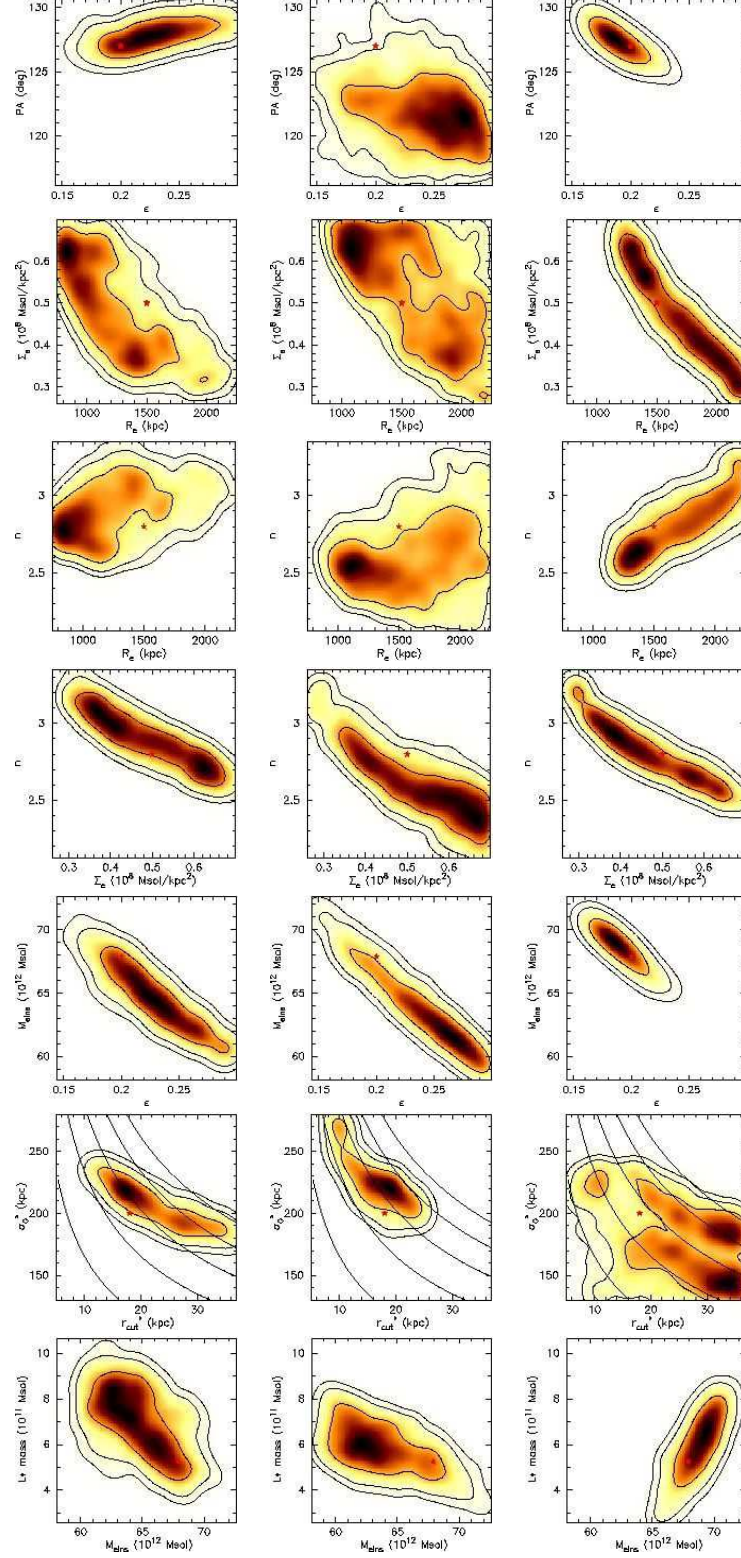


**Figure 6.** 2D Posterior distributions of the parameters of the cluster-scale halo modelled with a Sérsic potential obtained from left to right with Config. 1, 2 and 3 of multiple images respectively. The 3 contours stand for the  $1\sigma$ ,  $2\sigma$  and  $3\sigma$  levels of confidence. The fiducial values are marked by the red star. The mass of a  $L^*$  galaxy is the total mass for a circular profiles. The cluster mass  $M_{eins}$  is the total enclosed mass (i.e. galaxy subhalos and cluster-scale halo) in the Einstein radius ( $30''$ ). The  $\chi^2$  was computed in the image plane.

**Table 5.** Sérsic parameters and mass estimations of the cluster-scale halo in 3 different strong lensing configurations. The parameters have been obtained with a  $\chi^2$  computed in the image plane. The errors are given at  $1\sigma$ . The  $L^*$  masses are given for a circular mass component with identical dynamical parameters.

	Fiducial	Config.1	Config.2	Config.3
$\epsilon$	0.2	0.23 $\pm 0.03$	0.24 $\pm 0.04$	0.19 $\pm 0.01$
$PA$ (deg)	127.	128.0 $\pm 0.8$	121.9 $\pm 2.3$	127.5 $\pm 1.0$
$R_e$ (kpc)	1500.	1195.7 $\pm 345.5$	1630.8 $\pm 372.4$	1698.5 $\pm 319.3$
$\Sigma_e$ ( $10^8 M_\odot$ )	0.5	0.5 $\pm 0.1$	0.5 $\pm 0.1$	0.5 $\pm 0.1$
$n$	2.8	2.9 $\pm 0.2$	2.6 $\pm 0.2$	2.8 $\pm 0.2$
$r_{cut}^*$ (kpc)	18.	21.0 $\pm 3.3$	16.8 $\pm 4.2$	25.4 $\pm 8.2$
$\sigma_0^*$ (km/s)	200.	206.6 $\pm 15.5$	223.6 $\pm 20.2$	178.0 $\pm 29.2$
$M_{L^*}$ ( $10^{11} M_\odot$ )	5.26	6.9 $\pm 1.3$	5.9 $\pm 0.9$	6.1 $\pm 1.2$
$M_{eins}$ ( $10^{12} M_\odot$ )	67.9	64.6 $\pm 2.0$	65.5 $\pm 3.4$	68.8 $\pm 1.3$

First, we note that in similar configurations, the Sérsic potential has more difficulties in recovering its fiducial parameters than do the PIEMD or the NFW potentials (we understand this because the effective radius and index parameters are mainly impacting the outer region of the mass distribution). This is evident for the PA fiducial value which falls only in the  $3\sigma$  contour of Config. 2.

Similarly as before, the ellipticity and the PA correlate together as well as with the cluster mass and the mass of a  $L^*$  galaxy.

We note that more than ever radial systems are required in order to recover the parameters correctly.

Figure 7 sums up the results found in this section concerning the precision obtained on the mass profile in each configuration for each potential. Although the accuracy of the recovery depends on image configurations it is almost always better than 5% in the region of multiple images with no obvious bias.

## 5. Model evaluation

In this section, we illustrate the use of the Bayesian evidence to select which parametric models are the best fit to the data. As an example, we consider the controversial slope of the central density profile in galaxy clusters. Sand et al. (2004) have used a sample of 6 galaxy clusters to show that the slope of the central density profile was shallower than  $r^{-1}$  as predicted by CDM simulations. However, they consider axially symmetric potentials. Bartelmann and Meneghetti (2004) reconsider these results and conclude that an NFW profile with  $r^{-1}$  inner slope could not be ruled out by strong lensing once effects of asymmetry and shear were taken into account.

Here, we consider a set of elliptical galaxy clusters modelled by a PIEMD potential i.e. with a core and an inner slope shallower than  $r^{-1}$ . We want to study how an SIE, an NFW and a Sérsic potential manage to fit a set of multiple images produced by such clusters and use the Bayesian evidence to select the best potential according to the data and the given priors. Our hypothesis is that even accounting for the effects of asymmetry and shear, an NFW profile cannot always reproduce a cluster with core.

We build 6 models of galaxy clusters with a cluster-scale halo described by a PIEMD potential whose core radius varies from 0 to 50 kpc. To account for asymmetry and shear, we append the same set of 78 perturbing galaxies as in the previous section

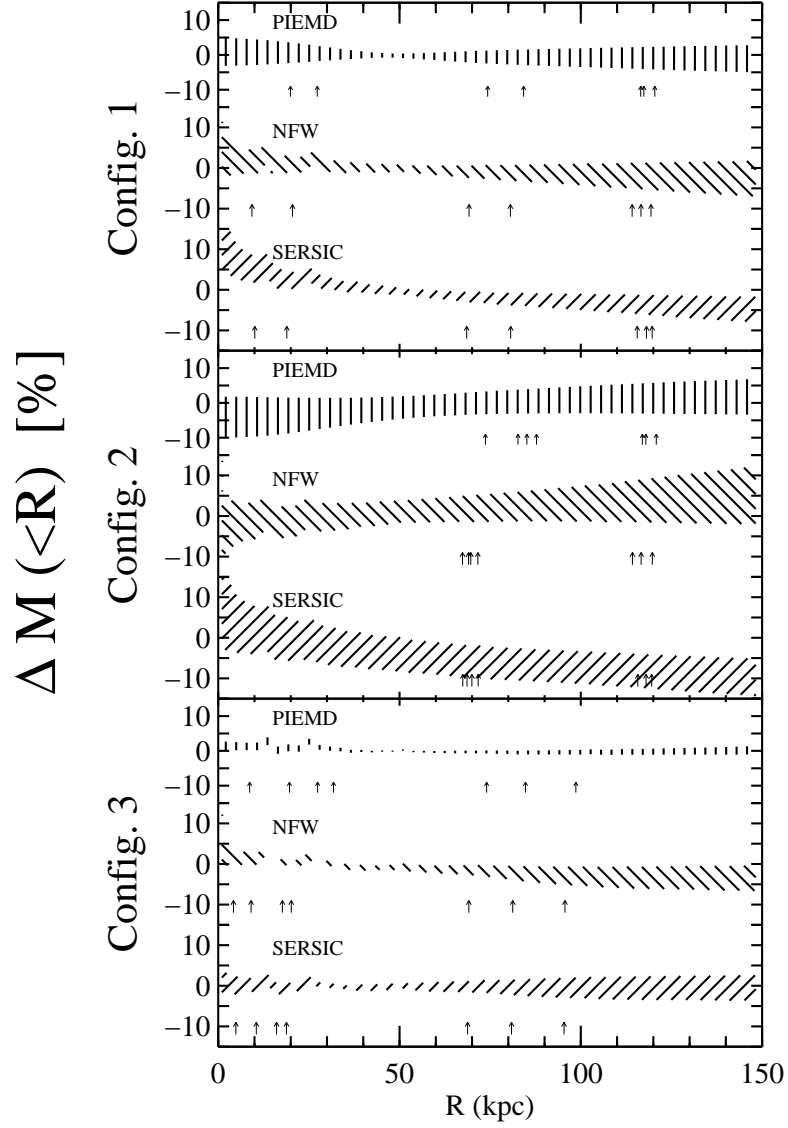


**Figure 7.** Relative mass profiles recovery in the three configurations for the three potentials PIEMD(vertically hatched region), NFW( $-45^\circ$  hatched region) and Sersic( $45^\circ$  hatched region). The arrows below each plot mark the positions of the multiple images used as constraints. The error bars are given at  $1\sigma$ .



**Table 6.** Number of images and constraints per system and per simulation

Core radius (kpc)	Radial system images	Cusp system images	Constraints
0	2	4	8
10	2	4	8
20	2	4	8
30	3	5	12
40	3	3	8
50	5	3	12

and similarly as before, we sample the  $L^*$  galaxy parameters  $r_{cut}^*$  and  $\sigma_0^*$ . The cD galaxy is described by a single PIEMD potential with the same characteristics as in the previous section.

By increasing the core radius of a PIEMD potential, the enclosed mass at a given radius increases. In order to build similar simulated clusters, we increase the velocity dispersion and the core radius at the same time so that the enclosed mass at the Einstein radius is the same in each simulated cluster.

In the previous section, we have highlighted parameters degeneracies for the PIEMD, the NFW and the Sérsic potentials. However, we do not know for instance up to what point the concentration of the NFW potential changes when the core radius of a PIEMD potential grows or shrinks. Therefore, we consider uniform priors for each parameter with limits large enough so that the best fit region falls inside the limits. We assume that with such “undefined” priors, it will be possible to compare the evidences between each fitted model.

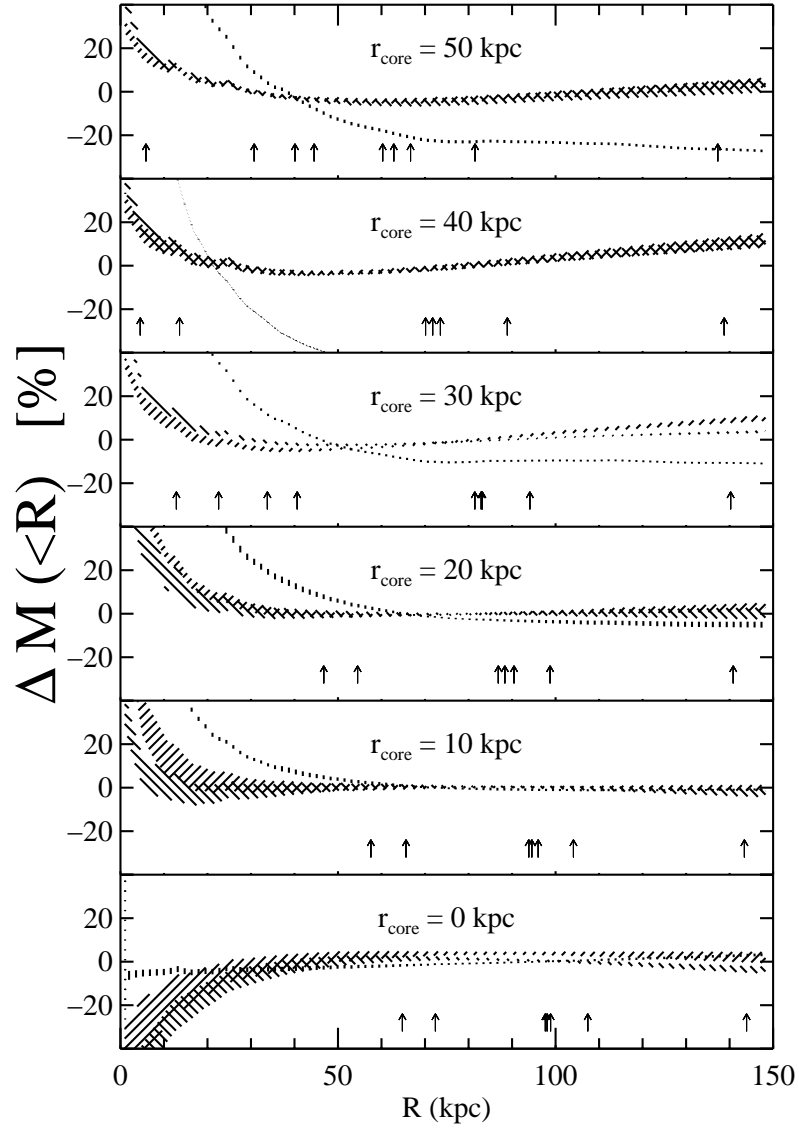
In order to constrain properly the shape of the density profile, we build 6 sets of multiple images similar to the Config. 1 i.e. 1 system singly imaged, 1 radial system and 1 cusp system. However, for models with  $r_{core} < 30$  kpc, we had to remove the desampled images produced at the very centre of the mass distribution since they are never observed because too faint or blended in the cD galaxy flux. As we previously did, we added a Gaussian noise of FWHM 0.1” to each image position. The number of images for each source is reported in Table 6.

Figure 8 shows the mass profile errors relative to fiducial PIEMD mass profiles for the SIE, the NFW and the Sérsic potentials. The arrows mark the positions of the multiple images used as constraints. The outer arrows correspond to the position of the singly imaged systems. Their constraints on the enclosed mass are weak as shown by the large deviation from the fiducial mass profile in the cases where  $r_{core} \geq 30$  kpc.

The triplets of nearby arrows mark the position of the giant arcs and counter-images of the cusp systems. Their distances from the centre decrease when the core radius increases. In fact, Kneib et al. (1993, Equation (3.46)) has shown that the radius of the tangential and radial critical lines decrease when the core radius increases. We clearly note that the mass profiles are well constrained only within the radius enclosed by the giant arcs of the cusp systems even when fitting a model with a large core radius.

At smaller radius, the intrinsic inner slope of each potential (see also Figure B1 for the absolute shape) makes the mass profile strongly deviate from the fiducial PIEMD mass profile.

Note that for large core radius, the one parameter SIE model cannot recover the



**Figure 8.** Mass profiles errors relative to the fiducial PIEMD mass profiles for the fitted potentials SIE (vertically hatched region), NFW ( $-45^\circ$  hatched region) and Sérsic ( $45^\circ$  hatched region) as a function of the aperture radius. The arrows mark the positions of the multiple images used as constraints. The error bars are given at  $3\sigma$ .

**Table 7.** Comparison of the  $\log(\text{Evidence})$  produced by the fit of the NFW, SIE and Sérsic potentials to a core radius varying PIEMD potential. The values come from fits performed with sets of multiple images described in the text and a Rate equal to 0.1

Core radius (kpc)	$E_{NFW}$	$E_{Sersic}$	$E_{SIE}$	$E_{PIEMD}$
0	-27.	-25.	-28.	-20.
10	-25.	-23.	-33.	-19.
20	-27.	-24.	-146.	-19.
30	-198.	-204.	-1391.	-25.
40	-81.	-70.	-2795.	-19.
50	-86.	-73.	-3260.	-22.

mass profile accurately. In general using a wrong mass profile means that we have a larger inaccuracy that can reach generally up to 10% but even up to 20% with an SIE.

Table 7 gives the evidences produced by each potential in each simulation. Jeffreys (1961) provides a useful guide to what constitutes a significant difference between two models:  $1 < \Delta \ln E < 2.5$  is substantial,  $2.5 < \Delta \ln E < 5$  is strong, and  $\Delta \ln E > 5$  is decisive. Since the evidence of the SIE potential is always larger than the evidences of the NFW and the Sérsic potential, it can be easily ruled out. This is normal since no radial arc can appear with a SIE potential. An SIE potential cannot reproduce a cluster with core radius even accounting for asymmetries.

At small core radii, the NFW and the Sérsic potentials can reproduce sets of multiple images produced by clusters with core. Therefore, strong lensing cannot constrain properly the slope of the central density when no images fall inside the core radius.

However, when the innermost images become amplified and detectable, they appear at radii lower than the core radius and we note clearly that the evidences of both the NFW and the Sérsic models increase dramatically ruling out both models compared to the PIEMD model. In this case, the strong lensing can afford a constrain on the central density slope.

For higher core radius, both models are still ruled out compared to the PIEMD model but nonetheless, the Sérsic model evidence is better than the NFW evidence.

## 6. Discussion

In this study, we have described how to build a gravitational lensing model of galaxy clusters and a set of constraints with multiply and singly imaged systems. Then, we have presented a new Bayesian method for efficiently exploring its parameter space without falling into local maxima of the likelihood function. The Bayesian method also helps in measuring the errors with care including prior knowledge. We have illustrated the Bayesian posterior distribution analysis and the most likely estimates of the parameters by studying the degeneracies in the PIEMD, the NFW and the Sérsic potentials in 3 different configurations of multiple images. We draw the following conclusions.

(i) Strong degeneracies appear in both the PIEMD, the NFW and the Sérsic potentials. The parameters are clearly dependent and compensate in order to produce a constant enclosed mass at the images locations. The degeneracies are either due to the mathematical definitions of the potentials or to the configuration of multiple

images. The latter degeneracies are easily identified by looking at the degeneracies between the shape and the dynamical parameters.

(ii) As radial systems of multiple images constrain the very central part of the cluster, together with tangential arcs they provide unique constraints on the slope of the mass profile. It is therefore important to identify radial (or central) images in cluster cores.

(iii) The effective radius of the Sérsic profile is poorly constrained by strong lensing. It is only by combining strong and weak lensing that one can hope to better probe the effective radius. Similarly the cut radius of the PIEMD potential and the scale radius of the NFW potential are not well constrained by strong lensing only.

(iv) Every potential degenerate with the underlying set of galaxy-scale subhalos. In general, strong lensing alone is not able to disentangle properly the contribution of the galaxy-scale and the cluster-scale halos. By combining radial and tangential multiple image constraints a more accurate measurement of the mass profile is possible, thus allowing to constrain separately the cluster-scale halo and the galaxy-scale subhalos. Nevertheless, the cut-off radius of the  $L^*$  scaling galaxy is generally not properly constrained and remain with a 20% error. As shown by (Natarajan et al. 1998, 2006) combining weak and strong lensing constraints helps in better constraining cluster galaxies halos.

We have also illustrated the Bayesian inference using the evidences obtained by fitting a NFW, a Sérsic and a SIE potential to 6 PIEMD simulated clusters with different core radius. We have shown that the NFW and the Sérsic potentials can actually fit systems of multiple images produced by clusters with core radius *provided the core radius is smaller than the distance to the centre of the innermost multiple images*. For large core radius, additional radial images appear at the very centre of the cluster and provide strong constraints that can disentangle between the PIEMD, the NFW or the Sérsic potential.

Modeller must be aware of the degeneracies between the parameters of a given potential. The analysis in section 4 should help him/her in identifying immediately if the results of an optimization are real or are due to a mathematical degeneracy or a particular configuration of multiple images. In fact, this paper shows that strong lensing cannot constrain everything and the limitation of the modelling are strongly dependent of the multiple images configurations. For instance, it is not possible to constrain the central density slope without radial images. Actually, the presence of radial images strongly suggest the presence of a shallow core.

In a forthcoming paper, we will expand this method to constrain cosmological parameters with strong lensing. With a large number of multiple images with known redshift, one should be able to compare the strong lensing cosmography constraints (similarly to the early work of Golse et al. (2002) and Soucail et al. (2004)) with other methods such as the CMB/WMAP results, or Supernovae or cosmic shear results.

## Acknowledgments

We acknowledge Bernard Fort and Alain Smette for their support and their useful comments. We thank John Skilling for allowing us to use his BAYESYS MCMC sampler. JPK acknowledge support from CNRS and CNES. This work was supported in part by the European Community's Sixth Framework Marie Curie Research Training Network Programme, Contract No. MRTN-CT-2004-505183 "ANGLES". The Dark Cosmology Centre is funded by the Danish National Research Foundation.

## References

- Abdelsalam H M, Saha P and Williams L L R 1998 *MNRAS* **294**, 734–+.
- Bardeau S, Kneib J P, Czoske O, Soucail G, Smail I, Ebeling H and Smith G P 2005 *A&A* **434**, 433–448.
- Bartelmann M and Meneghetti M 2004 *A&A* **418**, 413–418.
- Blandford R and Narayan R 1986 *ApJ* **310**, 568–582.
- Broadhurst T, Benítez N, Coe D and et al 2005 *ApJ* **621**, 53–88.
- Cabanac R A, Alard C, Dantel-Fort M, Fort B, Gavazzi R, Gomez P, Kneib J P, Le Fèvre O, Mellier Y, Pello R, Soucail G, Sygnet J F and Valls-Gabaud D 2007 *A&A* **461**, 813–821.
- Caon N, Capaccioli M and D’Onofrio M 1993 *MNRAS* **265**, 1013–+.
- Ciotti L 1991 *A&A* **249**, 99–106.
- Ciotti L and Bertin G 1999 *A&A* **352**, 447–451.
- Clowe D, Bradač M, Gonzalez A H, Markevitch M, Randall S W, Jones C and Zaritsky D 2006 *ApJ* **648**, L109–L113.
- Clowe D and Schneider P 2001 *A&A* **379**, 384–392.
- Comerford J M and Natarajan P 2007 *ArXiv Astrophysics e-prints* .
- Corless V and King L 2006 *ArXiv Astrophysics e-prints* .
- de Propriis R, Stanford S A, Eisenhardt P R, Dickinson M and Elston R 1999 *AJ* **118**, 719–729.
- Diego J M, Sandvik H B, Protopapas P, Tegmark M, Benítez N and Broadhurst T 2005 *MNRAS* **362**, 1247–1258.
- Dominik M 1995 *Astronomy and Astrophysics, Supplement* **109**, 597–+.
- Elíasdóttir Á, Möller O and in prep. 2007.
- Faber S M and Jackson R E 1976 *ApJ* **204**, 668–683.
- Freedman D and Diaconis P 1981 *Probability Theory and Related Fields* **57**, 453–476.  
**URL:** <http://www.springerlink.com/content/mp364022824748n3>
- Fritz A, Ziegler B L, Bower R G, Smail I and Davies R L 2005 *MNRAS* **358**, 233–255.
- Gavazzi R, Fort B, Mellier Y, Pelló R and Dantel-Fort M 2003 *A&A* **403**, 11–27.
- Golse G 2002 Strong Lensing PhD thesis Université Paul Sabatier, Toulouse III, France.
- Golse G and Kneib J P 2002 *A&A* **390**, 821–827.
- Golse G, Kneib J P and Soucail G 2002 *A&A* **387**, 788–803.
- Halkola A, Seitz S and Pannella M 2006 *MNRAS* pp. 1133–+.
- Hastings W 1970 *Biometrika* **57**, 97–109.
- Hilbert D 1891 *Mathematische Annalen* **38**, 459–460.
- Jeffreys H 1961 *Theory of Probability* 3 edn Oxford University Press.
- Jørgensen I, Franx M and Kjaergaard P 1996 *MNRAS* **280**, 167–185.
- Jullo E 2007 *in prep.* .
- Kassiola A and Kovner I 1993 *ApJ* **417**, 450–+.
- King L and Corless V 2007 *MNRAS* **374**, L37–L41.

- King L J, Clowe D I and Schneider P 2002 *A&A* **383**, 118–124.
- Kneib J, Hudelot P, Ellis R S, Treu T, Smith G P, Marshall P, Czoske O, Smail I and Natarajan P 2003 *ApJ* **598**, 804–817.
- Kneib J P, Ellis R S, Smail I, Couch W J and Sharples R M 1996 *ApJ* **471**, 643–+.
- Kneib J P, Mellier Y, Fort B and Mathez G 1993 *A&A* **273**, 367–+.
- Kochanek C S 2006 *in* G Meylan, P Jetzer, P North, P Schneider, C. S Kochanek and J Wambsganss, eds, ‘Saas-Fee Advanced Course 33: Gravitational Lensing: Strong, Weak and Micro’ pp. 91–268.
- Koopmans L V E, Treu T, Bolton A S, Burles S and Moustakas L A 2006 *ApJ* **649**, 599–615.
- Limousin M, Kneib J P, Bardeau S, Natarajan P, Czoske O, Smail I, Ebeling H and Smith G P 2007 *A&A* **461**, 881–891.
- Limousin M, Kneib J P and Natarajan P 2005 *MNRAS* **356**, 309–322.
- Limousin M, Richard J, Kneib J, Jullo E, Fort B, Soucail G, Elíasdóttir Á, Natarajan P, Smail I, Ellis R S, Czoske O, Hudelot P, Bardeau S, Ebeling H and Smith G P 2006 *ArXiv Astrophysics e-prints* .
- Lorensen W E and Cline H E 1987 *in* ‘SIGGRAPH’ pp. 163–169.
- Lynds R and Petrosian V 1986 *in* ‘Bulletin of the American Astronomical Society’ pp. 1014–+.
- Meneghetti M, Argazzi R, Pace F, Moscardini L, Dolag K, Bartelmann M, Li G and Oguri M 2007 *A&A* **461**, 25–38.
- Merritt D, Graham A W, Moore B, Diemand J and Terzić B 2006 *AJ* **132**, 2685–2700.
- Merritt D, Navarro J F, Ludlow A and Jenkins A 2005 *ApJ* **624**, L85–L88.
- Metropolis N, Rosenbluth A, Rosenbluth M, Teller A and Teller E 1953 *J. Chemical Physics* **21**(6), 1087–1092.
- Miralda-Escude J 1995 *ApJ* **438**, 514–526.
- Muñoz J A, Falco E E, Kochanek C S, Lehár J, McLeod B A, Impey C D, Rix H W and Peng C Y 1998 *Astrophysics and Space Science* **263**, 51–54.
- Natarajan P, De Lucia G and Springel V 2006 *ArXiv Astrophysics e-prints* .
- Natarajan P and Kneib J P 1997 *MNRAS* **287**, 833–847.
- Natarajan P, Kneib J P, Smail I and Ellis R S 1998 *ApJ* **499**, 600–+.
- Natarajan P, Loeb A, Kneib J P and Smail I 2002 *ApJ* **580**, L17–L20.
- Navarro J F, Frenk C S and White S D M 1997 *ApJ* **490**, 493–+.
- O Ruanaidh J J K and Fitzgerald W J 1996 *Numerical Bayesian methods applied to signal processing* Statistics and Computing Series Springer New York.
- Oguri M, Lee J and Suto Y 2003 *ApJ* **599**, 7–23.
- Paczynski B 1987 *Nature* **325**, 572–+.
- Press W H, Flannery B P and Teukolsky S A 1986 *Numerical recipes. The art of scientific computing* Cambridge: University Press, 1986.
- Richard J, Kneib J P, Jullo E, Covone G, Limousin M, Ellis R, Stark D, Bundy K, Czoske O, Ebeling H and Soucail G 2007 *ArXiv Astrophysics e-prints* .
- Saha P and Williams L L R 1997 *MNRAS* **292**, 148–+.

- Sand D J e a 2007 *in prep.* .
- Sand D J, Treu T, Smith G P and Ellis R S 2004 *ApJ* **604**, 88–107.
- Schneider P, Ehlers J and Falco E E 1992 *Gravitational Lenses* Gravitational Lenses, XIV, 560 pp. 112 figs.. Springer-Verlag Berlin Heidelberg New York. Also Astronomy and Astrophysics Library.
- Sérsic J L 1968 *Atlas de galaxias australes* Cordoba, Argentina: Observatorio Astronomico, 1968.
- Shaw L D, Weller J, Ostriker J P and Bode P 2006 *ApJ* **646**, 815–833.
- Simard L 1996 The Internal Kinematics of Intermediate Redshift Galaxies PhD thesis University of Victoria.
- Skilling J 2004 *BayeSys and MassInf.*  
**URL:** <http://www.inference.phy.cam.ac.uk/bayesys/>
- Smith G P, Kneib J P, Smail I, Mazzotta P, Ebeling H and Czoske O 2005 *MNRAS* **359**, 417–446.
- Soucail G, Fort B, Mellier Y and Picat J P 1987 *A&A* **172**, L14–L16.
- Soucail G, Kneib J P and Golse G 2004 *A&A* **417**, L33–L37.
- Soucail G, Mellier Y, Fort B, Mathez G and Cailloux M 1988 *A&A* **191**, L19–L21.
- Verdugo T, de Diego J A and Limousin M 2007 *ArXiv e-prints* **704**.
- Wambsganss J, Bode P and Ostriker J P 2005 *ApJ* **635**, L1–L4.
- Wuyts S, van Dokkum P G, Kelson D D, Franx M and Illingworth G D 2004 *ApJ* **605**, 677–688.

## Appendix A. Critical lines computation with Marching squares

A multiscale marching squares technique has been implemented in LENSTOOL to compute the critical lines. Marching squares is a computer graphics algorithm that generates contour lines for a 2D scalar field. It is similar to the marching cubes algorithm (Lorensen and Cline 1987). The algorithm proceeds through a scalar field taking four neighbour locations at a time (thus forming an imaginary square), then determining the line needed to represent the part of the contour that passes through this square. The individual lines are then fused into the desired contour.

This is done by creating an index to a precalculated array of 16 ( $2^4 = 16$ ) possible line configurations within the square (see Figure A1), by treating each of the 4 scalar values as a bit in an 4-bit integer. If the scalar’s value is higher than the iso-value (i.e. it is inside the contour) then the appropriate bit is set to one, while if it is lower (outside), it is set to zero. The final value after all 4 scalars are checked, is the actual index to the line configuration array.

In the critical lines case, the scalar field is not known a-priori. Therefore, we adopt a multiscale algorithm to focus towards the critical lines. The field is split in two recursively until we reach a higher limit for the size of a rectangle. Then, if a critical line is detected in a rectangle, it is split further. The rectangles with no critical line detected are left aside. Once the size of the rectangle has reached a lower limit, a line is kept in memory for this rectangle according to the marching squares configurations. The individual lines are then fused into the critical lines contour.

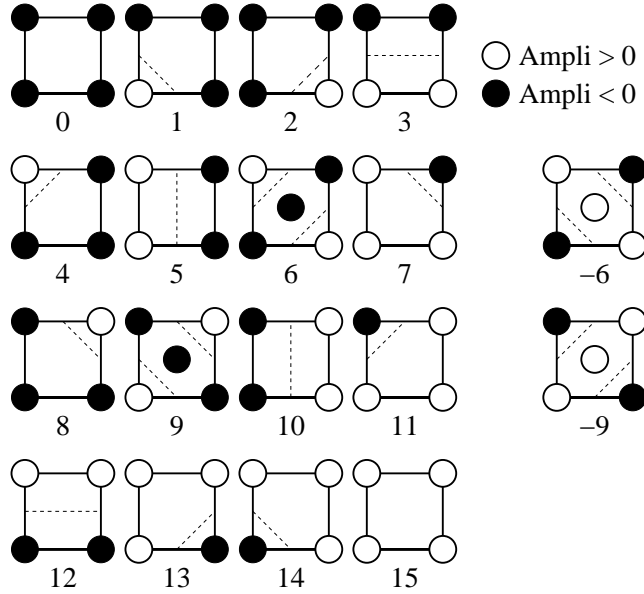


**Figure A1.** 16 square configurations. The empty and filled circles are points with positive and negative amplification respectively. The dashed lines are the inferred critical lines.

The previous technique was a line following algorithm called SNAKE. It starts from the center of a clump and picks amplification samples along its way outwards. When an amplification sign change is encountered, it precises the infinite amplification position and circles the clump until it comes back to its starting point along the critical line.

In complex environment, the SNAKE algorithm sometimes gets lost and produces incomplete critical lines. Conversely, the multiscale marching square algorithm never gets lost and identifies all the critical lines in the field. However, it can miss a part of critical line if the higher limit is too large.

## Appendix B. Pseudo-elliptical Sérsic potential

As another addition to LENSTOOL, we have incorporated the Sérsic density profile (Sérsic 1968) as an alternative description of the matter density. The motivation for including it is that as the Sérsic profile describes the 2D luminosity profile of elliptical galaxies (Sérsic 1968; Ciotti 1991; Caon et al. 1993), it can be used to separately model the baryonic matter component (which should be traced by the light) and the dark matter (DM) component, given enough lensing constraints. In addition, Merritt et al. (2005, 2006), find that a deprojected Sérsic profile gives a better fit than an NFW profile to the 3D density profile of DM halos from simulations. Elíasdóttir et al. (2007) found that given that the surface density distribution is indeed given by a Sérsic profile, but fitted by an NFW using lensing constraints, it can lead to unrealistic estimates of the parameters (e.g. the predicted weak lensing signal and the concentration parameter), making the Sérsic profile an interesting alternative for modelling the DM



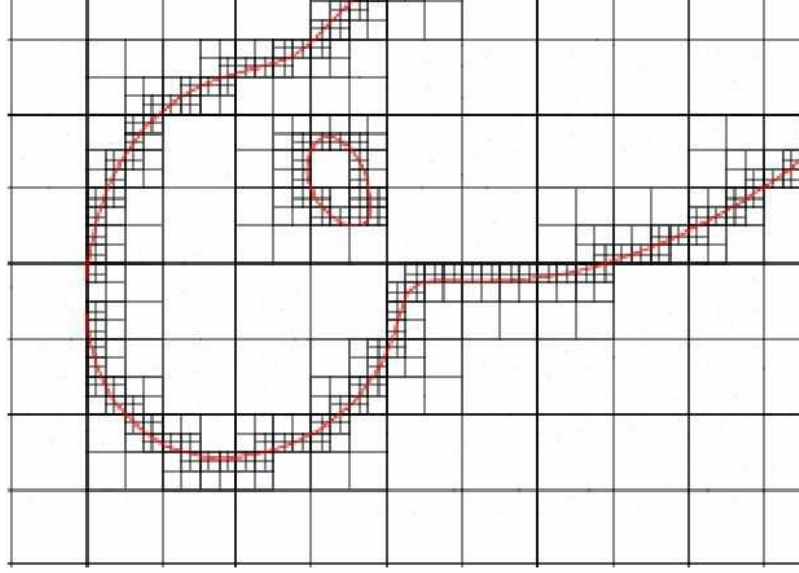


**Figure A2.** Multiscale marching square field splitting. The boxes represent the splitting squares and the red lines, the critical curve contour. The imposed upper and lower limits for the boxes sizes are 10'' and 1'' respectively. The 1'' boxes are not plotted for clarity.

halos themselves. Finally, the special case of the Sérsic index  $n = 1$ , corresponds to an exponential disk, making it useful for modelling spiral galaxies. Spiral lenses are comparatively rare to date, but dedicated efforts are being made to find such lenses, and with the inclusion of the Sérsic profile to Lenstool, it can now be used to study and model such lenses.

The Sérsic 2D density profile has three free parameters  $(n, R_e, \Sigma_e)$  and is given by:

$$\Sigma_{\text{ser}} = \Sigma_e \exp \left[ -b_n \left( \left( \frac{R}{R_e} \right)^{1/n} - 1 \right) \right], \quad (\text{B.1})$$

where  $R$  is the projected radius,  $n$  is the Sérsic index,  $b_n$  is a constant chosen such that  $R_e$  is the radius containing one-half of the projected mass and  $\Sigma_e$  is the density at  $R_e$ . The Sérsic profile reduces to the de Vaucouleurs profile for  $n = 4$ , and to the exponential disk for  $n = 1$ . The other parameters of the Sérsic profile in LENSTOOL are its position on the sky, its position angle and its ellipticity. In Figure B1, we compare the surface density of the Sérsic, the NFW and the PIEMD profiles both in the very central and in the very outer regions. These regions are accessible either to strong or weak lensing.

The elliptic version of the Sérsic profile is calculated using the pseudo-elliptical approximation developed by Golse et al. (2002). It is introduced in the expression of the circular Sérsic potential by substituting  $R$  by  $R_e$ , using the following elliptical

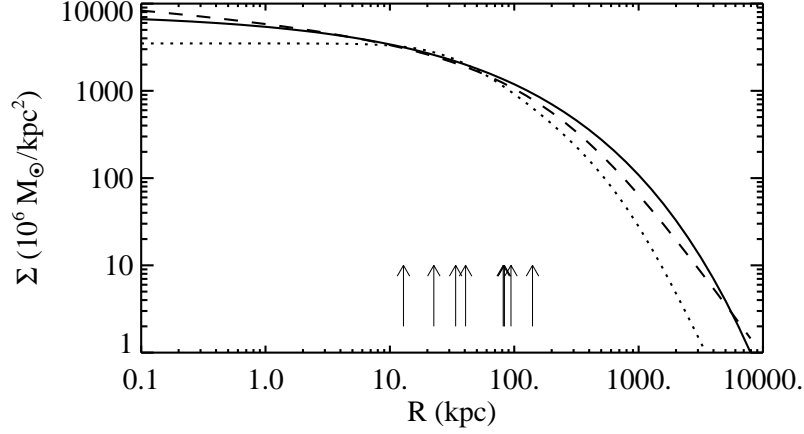


**Figure B1.** Surface density comparison between the Sérsic profile (solid line), the NFW profile (dashed line) and the PIEMD potential (dotted line). The surface densities correspond to the fit performed in section 5 and extended to very small and large radii. The arrows mark the multiple images positions used as constraints.

coordinate system:

$$\begin{cases} x_\epsilon = \sqrt{(1-\epsilon)}x \\ y_\epsilon = \sqrt{(1+\epsilon)}y \\ R_\epsilon = \sqrt{x_\epsilon^2 + y_\epsilon^2} \\ \phi = \arctan(y_\epsilon/x_\epsilon). \end{cases} \quad (\text{B.2})$$

In this definition,  $\epsilon = (a^2 - b^2)/(a^2 + b^2)$  where  $a$  and  $b$  are respectively the semi-major and the semi-minor axis of the elliptical potential. From the elliptical lens potential  $\varphi_\epsilon(r) \equiv \varphi(r_\epsilon)$ , Golse et al. propose generic expressions to compute the elliptical deviation angle  $\alpha_\epsilon(\mathbf{r})$ , the convergence  $\kappa_\epsilon(\mathbf{r})$ , the shear  $\gamma_\epsilon(\mathbf{r})$  and the projected mass density  $\Sigma_\epsilon(\mathbf{r})$ :

$$\Sigma_\epsilon(\mathbf{r}) = \Sigma(r_\epsilon) + \epsilon \cos 2\phi_\epsilon (\bar{\Sigma}(r_\epsilon) - \Sigma(r_\epsilon)). \quad (\text{B.3})$$

The pseudo-elliptical developments are limited to small ellipticities. For instance for the NFW, when  $\epsilon > 0.25$ , the surface iso-densities become increasingly boxy/peanut. Similarly for the Sérsic potential, we have found that when  $\epsilon > 0.25$ , the goodness of fit (defined in Golse et al.) measured at  $R_\epsilon = R_e$  becomes larger than 10%. We also fit the relation between  $\epsilon_\Sigma$  and  $\epsilon$  and found  $\epsilon_\Sigma = 3.55\epsilon - 3.42\epsilon^2$  with a  $\chi^2 = 10^{-5}$ .

The ellipticities of the potentials used in this paper and of the projected mass densities  $\epsilon_\Sigma$  are linearly proportional through multiplicative factors (reported in Table 1).

The range of valid surface density axis ratio  $q = b/a$  provided by the pseudo-elliptical approximation for the SIE, the NFW and the Sérsic potentials are  $q_{SIE} > 0.65$ ,  $q_{NFW} > 0.53$  and  $q_{Sersic} > 0.44$  respectively. From N-body simulations Oguri et al. (2003) found that the most probable projected axis ratio is  $q = 0.6$ . The pseudo-elliptical technique is therefore able to model most of the triaxial halos.

In case of highly elliptical mass distributions, the PIEMD model (Kassiola and Kovner 1993) produces elliptical iso-densities because the ellipticity has been introduced directly in the projected mass distribution and not at the level of the potential.